The Aeronautical Journal (2026), **130**, pp. 2528–2557
doi:10.1017/aer.2026.10186

ROYAL AERONAUTICAL SOCIETY

RESEARCH ARTICLE

Synergistic flow control for coupled internal–external flows in semi-embedded wing-intake configurations

Bolin Ma, Yuanhua Liu, Lanting Li, Tianyu Gong and Wei Yuan

Beihang University, China
Corresponding author: Wei Yuan; Email: yuanwei@buaa.edu.cn

Received: 22 January 2026 UTC; **Revised:** 30 April 2026 UTC; **Accepted:** 30 April 2026 UTC

Keywords: boundary layer ingestion; flow control; internal/external coupling flow; jet flow; suction

Abstract

Blended-wing-body (BWB) aircraft with distributed propulsion offers significant potential for aerodynamic efficiency. However, this tightly integrated configuration inherently operates under boundary layer ingestion (BLI) conditions. The ingested thick fuselage boundary layer, coupled with the strong aerodynamic interactions between the S-shaped intake and wing, generates adverse pressure gradients at the inlet alongside low total pressure recovery coefficients and high outlet distortion. This study investigates integrated flow control under high-altitude flight conditions using a BWB aerofoil integrated with a semi-embedded S-shaped intake model, incorporating energy analysis. During cruise, strong adverse pressure gradients between the wing shock wave and intake cause distinct lip separation, resulting in a low total pressure recovery coefficient and high distortion. Distributed dual-row suction generates secondary flow generates distributed secondary flow near the separation point with equivalent energy consumption. This enhances fuselage boundary layer mixing, reduces near-wall adverse pressure gradients and improves the total pressure recovery coefficient. The integration of internal jet control synergistically augments the benefits of external wing suction via distinct spatial mechanisms: central jets replenish core flow kinetic energy to suppress separation and improve the total pressure recovery coefficient, while side jets enhance mixing between separation zones and mainstream flow, mitigating secondary swirl losses and substantially reducing distortion at the aerodynamic interface plane (AIP). Energy analysis confirms that a modest energy input (equivalent to 7.4% of the mainstream kinetic energy) yields a significant increase in intake thrust, while simultaneously reducing total pressure and swirl distortion.

Nomenclature

BWB	blended wing body
BLI	boundary layer ingestion
APG	adverse pressure gradients
AIP	aerodynamic interface plane
Ma	Mach number
D_{out}	intake exit diameter
L	aerofoil chord length
L	distance from the upper wing surface to the intake lip
X	dimensionless distance l/L
DC (150)	total pressure distortion
SC (150)	swirl distortion
$\overline{P_t}$	average total pressure
v	flow velocity
v_{CF}	swirl velocity in 150° sector
D_P	normalised wall pressure differential
P	static pressure

© The Author(s), 2026. Published by Cambridge University Press on behalf of Royal Aeronautical Society.

https://doi.org/10.1017/aer.2026.10186 Published online by Cambridge University Press

C_μ	jet momentum coefficient
$\dot{m}_j$	jet mass flow rate
U_j	jet velocity
P_j	power consumption coefficient of jet area
P_s	power consumption coefficient of suction
$\Delta P_\mathrm{suction}$	pressure difference acting on the suction process
$\dot{m}_\mathrm{s}$	suction flow rate
U_e	mainstream streamwise velocity

Greek symbol

σ	total pressure recovery coefficient
ρ	local atmospheric density

1.0 Introduction

In the domain of civil aviation design, advancements in the integration of airframe and propulsion systems have accelerated. The blended wing body (BWB) configuration stands out as a viable solution for achieving substantial performance benefits, including reduced noise emissions and improved fuel efficiency [1–6]. Its reduced wetted surface area minimises skin friction drag, while its seamlessly integrated, compact aerodynamic design effectively suppresses pressure drag [7–9]. The core of this configuration is the S-shaped intake, which acts as a vital component for coupling the external airflow with the propulsion system and helps the engine to be embedded into the fuselage. This design synergistically enhances aerodynamic and propulsive efficiency by enabling boundary layer ingestion (BLI) from the fuselage surface through the S-shaped intake geometry [10–12].

Significant coupling effects exist between the airframe and intake systems in distributed propulsion configurations. When the engine is tightly integrated with the aircraft, the ingestion of fuselage boundary layer airflow reduces upper-surface pressure and alters external flow patterns. Experimental and numerical studies by Aaron T. Perry [13] and Michael Kerho [14] independently demonstrated that flow blockage and spillage phenomena occur at nacelle lips under BLI-affected conditions due to engine operating states. Vladislav et al. [15] further coupled BWB aircraft configurations with propulsion systems, revealing that engine states actively modify wing pressure distributions and boundary layer development, directly influencing pressure recovery coefficient and lift generation. Their work also identified critical impacts of intake size/position on lift performance and intake losses. Kim [16, 17] and Xiang [18] conducted nacelle and fuselage shape optimisation to address these coupled flow interactions: Kim implemented a volume force model for airframe-engine integration and applied adjoint-based methods to refine nacelle geometry, reducing shock intensity and boundary layer separation; Xiang quantified geometric sensitivities via Morris analysis, identifying maximum nacelle cross-section thickness as a dominant aerodynamic coupling parameter.

Meanwhile, the internal flow field undergoes significant alterations after engine ingestion of boundary layers. Plas et al. [6] experimentally demonstrated that BLI reduces fuel consumption by several percentage points, albeit with detrimental engine effects. Ferrar [19], Florea [20] and Thouault [21] numerically studied S-shaped intake flow characteristics under BLI: Ferrar emphasised static pressure gradients as the governing factor for internal flow evolution, while Florea revealed that intake velocity deficits from fuselage boundary layers induce inhomogeneous intake conditions, generating severe total pressure losses. Near the inner wall of the S-intake, flow separation occurs under high-curvature conditions, amplifying total pressure loss regions to occupy ∼50% of the cross-sectional height at the fan inlet. Beyond flow separation, adverse pressure gradients along the duct reduce total pressure recovery coefficients at the outlet and exacerbate total pressure and swirl distortion – BLI further intensifies these distortions. Consequently, compressor performance degrades (reduced maximum pressure ratios and efficiency [22]) and the blades are subjected to cyclic loads from a circumferentially non-uniform flow, leading to forced vibration-induced fatigue failures. Thus, strategies are needed to mitigate these effects

https://doi.org/10.1017/aer.2026.10186 Published online by Cambridge University Press

while retaining BLI advantages, and current efforts focus on flow control in S-ducts to promote mixing and weaken distortion impacts.

Researchers have developed passive and active flow control strategies to combat strong adverse pressure gradients and secondary flows in the S-intake. Passive control primarily employs vortex generators (VGs). As early as 1985, Vakili et al. [23] experimentally analysed secondary flow suppression mechanisms in S-intake using targeted VGs, revealing their roles in causing lateral flow in high/low-pressure zones, reducing secondary flow losses and delaying boundary layer separation. Optimal performance required coordinated design of vortex generator height, angle, quantity and boundary layer extraction height [24, 25]. In contrast, active control introduces external energy into the flow. Ferrar et al. [19] designed a jet actuation system, demonstrating that placement at the BLI intake and duct exit (jet mass flow $\leq$2% of intake flow) achieved 30% reductions in outlet distortion, simultaneously improving stall margin and engine performance. Harrison et al. [26] redistributed low-momentum boundary layer fluid via suction, showing that pure suction fails to mitigate distortion, but the blowing with a blowing ratio $>$1% enhances anti-distortion capabilities. Debiasi et al. [27] validated consistent results through simulations: blowing/suction improved separation in dual-bend ducts, increased total pressure recovery coefficient and reduced distortion using only 2% mainstream energy. R. Mathis et al. [28] experimentally applied synthetic jet actuators (orifice outlets) to a 2D S-intake model with a high-curvature inlet. The particle image velocimetry (PIV) data showed that without control, a large boundary layer separation zone formed in the curved section, while synthetic jets induced complete boundary layer reattachment.

Despite these advancements, existing studies predominantly treat external wing aerodynamics and internal intake flows as isolated systems. However, in distributed propulsion configurations, the shock-induced boundary layer separation on the wing upper surface is strongly coupled with the secondary flow development within the S-shaped intake. This complex aerodynamic interaction renders isolated control strategies – relying solely on either external suction or internal jet injection – inefficient, as they fail to address the global flow physics.

This study proposes an integrated synergistic control strategy to address this critical gap. Moving beyond the simplistic superposition of suction and jet techniques, this work investigates the underlying mechanism of how external suction can fundamentally reconfigure the ingested boundary layer topology. By effectively mitigating the upstream shock-induced separation, the external control preconditions the flow, enabling the internal jets to suppress core separation and swirl distortion with a significantly reduced momentum coefficient. This research highlights the distinct innovation of coupled internal–external flow control over traditional single-domain approaches, offering a systematic framework for maximising the aerodynamic efficiency of distributed propulsion systems.

In conclusion, BLI propulsion systems offer clear advantages but face challenges in mitigating engine inlet distortions under strong airframe-propulsion coupling. While significant progress has been made in S-intake flow control, integrated analyses of distributed wings with S-intakes remain lacking. Fundamental understanding of coupled external–internal flow mechanisms is insufficient, and systematic design/optimisation frameworks are absent. This study addresses these gaps by numerically investigating wing-intake interactions using a large civil aircraft airframe-intake coupled model. Combined flow control strategies – wing boundary layer extraction and duct jet actuation – are applied to synergistically mitigate total pressure and swirl distortions at the aerodynamic interface plane (AIP), with subsequent optimisation of control mechanisms. Furthermore, an energy analysis is conducted to weigh the aerodynamic performance gains against the energy costs of the flow control system.

2.0 Methodology

2.1 Baseline model

The research object of this study is a coupled model of a geometric aerofoil section from a large commercial aircraft and its corresponding semi-embedded S-shaped intake. The selected 3D aircraft model is shown in Fig. 1, with multiple fans embedded in the rear fuselage and distributed along the spanwise direction. To simplify the model, a specific cross-section was extracted along the fuselage spanwise

https://doi.org/10.1017/aer.2026.10186 Published online by Cambridge University Press

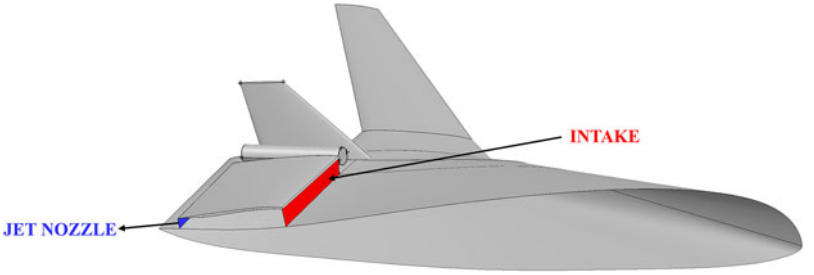


Figure 1. *Aircraft 3D model.*



Figure 2. *Coupling structure of the wing and intake.*

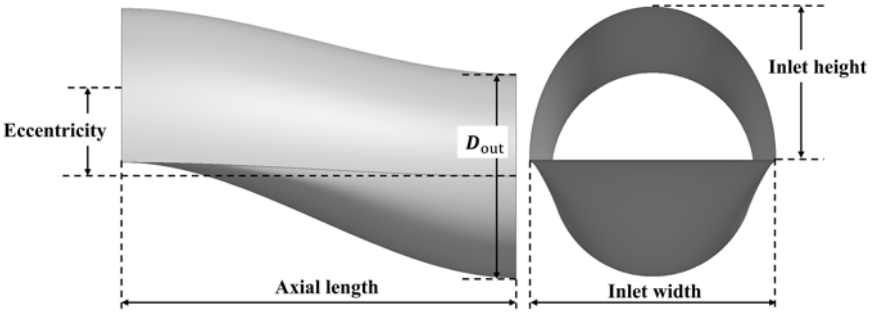


Figure 3. *Intake model.*

direction, and the aerofoil section was extended spanwise to form a coupled analysis model with the intake. Figure 2 illustrates the schematic of the coupled wing-intake structure. The intake model employs a D-shaped entrance semi-embedded S-intake, with its geometric configuration shown in Fig. 3 and dimensional parameters listed in Table 1. All geometric parameters are normalised by the intake exit diameter D_{out}.

The computational domain and mesh for the coupled aerofoil-intake system are displayed in Fig. 4. The far upstream serves as the inlet boundary, both sides are symmetric boundaries, and the remaining boundaries are open. Since no fan or nozzle structure was incorporated downstream of the intake outlet, the computational domains of the upper and lower parts of the aerofoil at the rear of the intake are disconnected. The distances to the upper, lower, front and rear boundaries of the computational domain are all set to 40 times the aerofoil chord length L, while the lateral boundaries are located at $8L$.

2.2 Numerical method and independence check

Steady-state computational fluid dynamics (CFD) simulations were performed using ANSYS CFX (Release 18.2) to solve the Reynolds-averaged Navier-Stokes (RANS) equations. The governing equations for conservation of mass, momentum and total energy are expressed in Cartesian tensor form as follows:

$$\frac{\partial(\rho u_i)}{\partial x_i} = 0 \tag{1}$$

https://doi.org/10.1017/aer.2026.10186 Published online by Cambridge University Press

Table 1. *Basic geometric parameters of the intake*

Parameters	Value
Intake width/D_{out}	1.21
Intake height/D_{out}	0.75
Axial length/D_{out}	1.43
Eccentricity/D_{out}	0.41

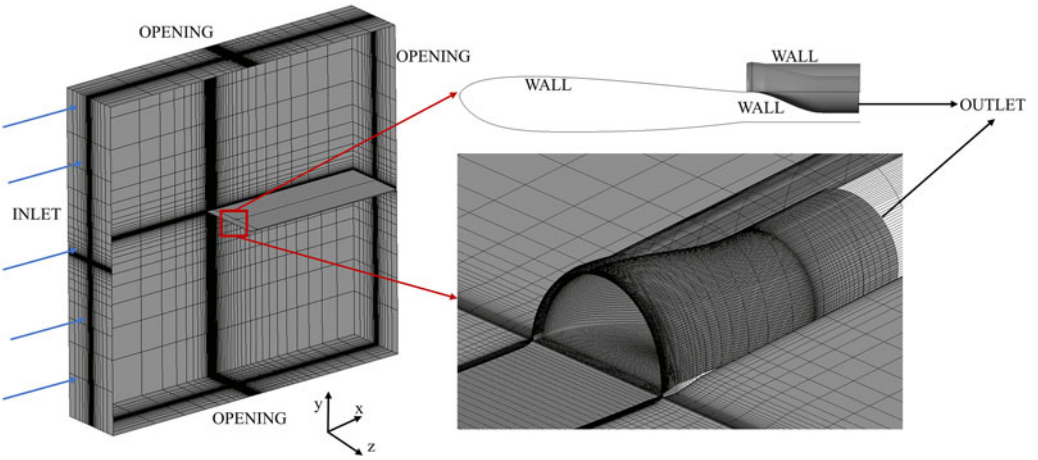


Figure 4. *Grid of coupling structure.*

$$\frac{\partial\left(\rho u_i u_j\right)}{\partial x_i}=-\frac{\partial p}{\partial x_i}+\frac{\partial}{\partial x_j}\left[\mu\left(\frac{\partial u_i}{\partial x_j}+\frac{\partial u_j}{\partial x_i}-\frac{2}{3}\delta_{ij}\frac{\partial u_k}{\partial x_k}\right)-\rho\overline{u_i' u_j'}\right] \tag{2}$$

$$\frac{\partial}{\partial x_j}\left[u_j\left(\rho E+p\right)\right]=\frac{\partial}{\partial x_j}\left[\left(\lambda+\lambda_t\right)\frac{\partial T}{\partial x_j}+u_i\left(\tau_{ij}-\rho\overline{u_i' u_j'}\right)\right] \tag{3}$$

To close the compressible system, the ideal gas law is utilised: $p=\rho RT$, where ρ, u, p, T and E denote the fluid density, time-averaged velocity component, static pressure, temperature and total energy, respectively. μ and λ are the dynamic viscosity and thermal conductivity, whereas λ_t represents the turbulent thermal conductivity. The term $-\rho\overline{u_i' u_j'}$ represents the Reynolds stress tensor, which is modeled to close the governing equations. In this study, the shear-stress transport (SST) turbulence closure model was employed to accurately capture the shock-boundary layer interactions and flow separation phenomena.

The computational domain encompassing both the external flow field and integrated aerofoil-intake configuration was discretised using ANSYS ICEM CFD (Release 18.2) software, incorporating local grid refinement near the aerofoil leading edge and intake walls to maintain a first-layer grid height of 5×10^{-6}m. To verify the near-wall resolution requirements for the SST turbulence model, the y^+ distribution along the solid surfaces is evaluated. As illustrated in Fig. 5, the y^+ values are strictly maintained below 2 across the entire computational domain, with the vast majority of the aerodynamic surfaces achieving $y^+<1$. This fine near-wall resolution ensures that the viscous sublayer is accurately resolved, meeting the stringent requirements for predicting boundary layer separation and shockwave interactions.

The numerical setup replicated cruise conditions at an altitude of 11 km (Mach 0.85). To ensure clarity and convergence stability, the detailed boundary conditions are summarised in Table 2. The boundary

https://doi.org/10.1017/aer.2026.10186 Published online by Cambridge University Press

Table 2. *Boundary conditions for the numerical simulation*

Boundary region	Boundary type	Parameters
Domain Inlet	Inlet	Normal speed = 250 m/s, Total temperature = 248 K
Far-field (Upper, Lower, Rear)	Opening	Static pressure = 22,700 Pa, Static temperature = 217 K
Intake Exit	Outlet	Static pressure = 20,000 Pa
Solid Walls	Wall	No-slip, Adiabatic

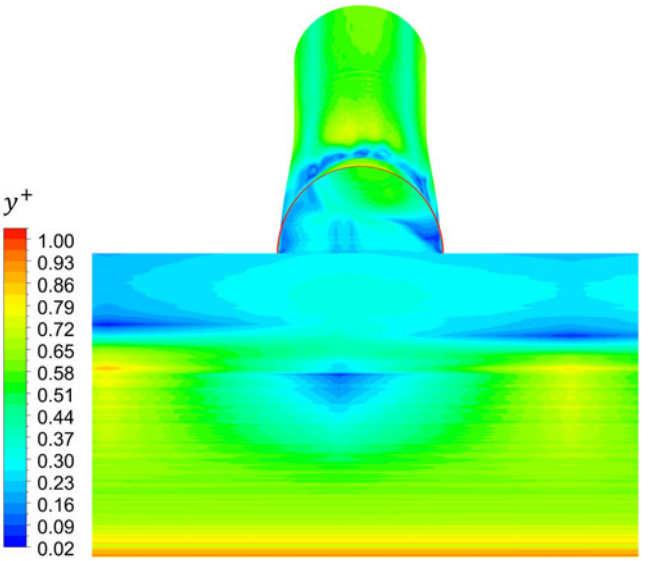


Figure 5. *Contour of* y^+ *distribution on the wing and S-shaped intake surfaces.*

positions and boundary types in Table 2 are shown in Fig. 4. The domain inlet was assigned a prescribed axial velocity of 250 m/s and a static temperature of 248 K. The far-field boundaries (including upper, lower and domain rear surfaces) were designated as Opening types (22,700 Pa, 217 K). For the intake exit, a fixed static pressure of 20,000 Pa was applied to match the design mass flow. Finally, adiabatic no-slip conditions were imposed on all solid walls.

Notably, the far-field boundaries (including the upper, lower and rear surfaces of the domain) were designated as Opening types. In the ANSYS CFX solver, the Opening boundary is functionally equivalent to the Pressure Far-Field condition used in other general CFD solvers. Unlike a standard pressure outlet that may cause numerical divergence if reverse flow occurs, the Opening boundary allows fluid to freely cross the boundary in either direction (inflow or outflow) based on the local pressure gradient. This configuration was specifically selected to mimic the unconfined freestream environment and accommodate simultaneous inflow and outflow phenomena at the domain edges, thereby ensuring computational accuracy and numerical stability.

Grid independence was established through systematic refinement studies involving four mesh resolutions (3.01–5.78 million cells). Figure 6 demonstrates the convergence behaviour of the total pressure distribution at the AIP. The corresponding total pressure contours at the AIP are embedded next to each data point. It shows that both the quantitative values and the qualitative flow topology stabilise once the cell count exceeds 4.12 million, confirming a grid-independent solution.

Additional aerodynamic parameters were extracted to verify convergence and further substantiate grid independence. As shown in Fig. 7, l denotes the distance from the fuselage upper surface to the

https://doi.org/10.1017/aer.2026.10186 Published online by Cambridge University Press

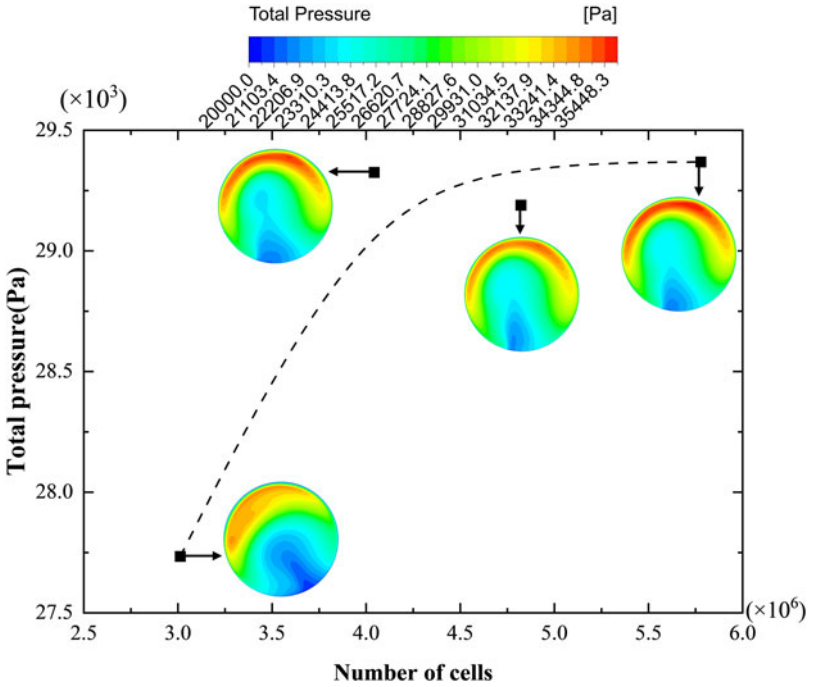


Figure 6. *Mass-averaged total pressure and corresponding total pressure contours at the AIP under different grid elements.*

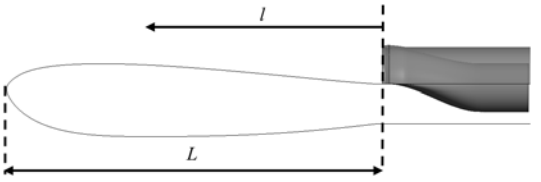


Figure 7. *Define the fuselage chord length L and the distance l in front of the intake lip.*

intake lip. l is non-dimensionalised as $X = l/L$, where L represents the wing chord length. Figure 8 illustrates the static pressure distribution on the wing's upper surface (a) and the streamwise velocity profile along the vertical axis at the intake lip (b) across different mesh resolutions. The results demonstrate that once the grid count exceeds 4.12 million, the variations in both the wing surface pressure and the intake inlet velocity profiles are negligible, indicating a grid-independent solution. This optimised mesh configuration was consequently adopted, providing an optimal compromise between numerical accuracy and computational efficiency.

2.3 Validation of numerical method

Since experimental data for the specific coupled wing-intake configuration in this study is currently unavailable, the numerical method (including the turbulence model and mesh strategy) was validated against the standard RAE M2129 S-duct experimental data [29] to ensure solver reliability. The RAE M2129 diffuser exhibits typical flow features of S-shaped intakes, including streamwise curvature-induced pressure gradients and secondary flow separation, which are consistent with the internal flow physics discussed in the present work.

The validation case utilised the same numerical setup described in Section 2.2: the ANSYS CFX solver with the SST turbulence model. The computational domain and boundary conditions replicated

https://doi.org/10.1017/aer.2026.10186 Published online by Cambridge University Press

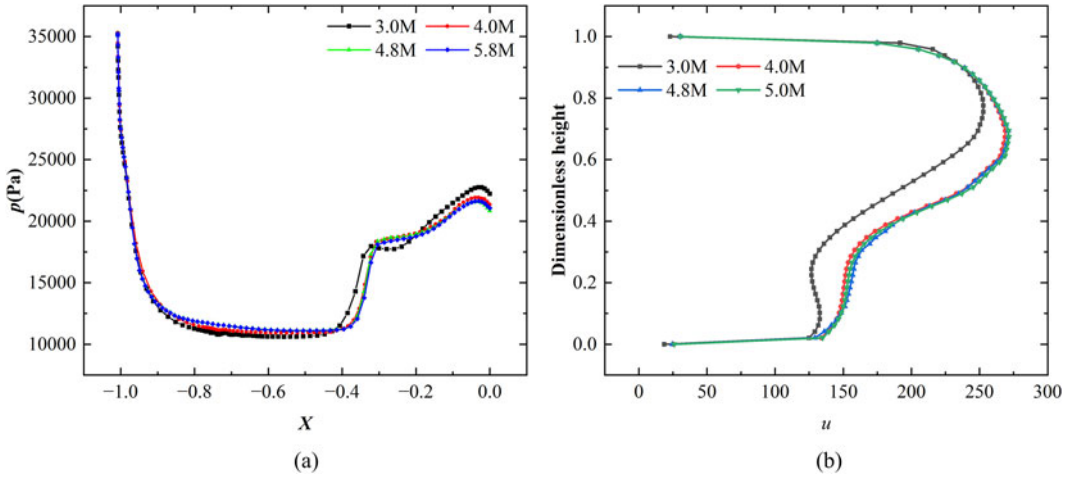


Figure 8. *Comparison of wing surface static pressure and lip velocity distribution with different grids: (a) static pressure distribution on the wing upper surface, and (b) streamwise velocity profile along the vertical axis at the intake lip.*

the experimental setup: an inlet Mach number of 0.6 and a Reynolds number of 2.6×10^6. The mesh topology and near-wall resolution ($y^+ < 1$) were kept consistent with the baseline model of this study to ensure grid similarity.

Figure 9 compares the computed wall static pressure distribution (where d is the inlet diameter, p is the wall static pressure, $p_{t,\,cl}$ and p_{cl} are the inlet total pressure and static pressure, respectively). As shown in Fig. 9, the numerical results for the static pressure coefficient along the duct centreline show excellent agreement with the experiment, with a maximum deviation of less than 2%. The calculations provided a good prediction of the variation trend of the pressure curve, and they can capture the separated flow region accurately.

The successful reproduction of the pressure distribution and secondary flow separation location in the Royal Aircraft Establishment (RAE) M2129 data confirms that the current numerical framework is capable of accurately capturing the complex internal flow structures and separation phenomena in S-shaped intakes.

2.4 Evaluating indicator

Two principal evaluation metrics are employed to quantitatively assess intake flow characteristics and flow control performance: the total pressure recovery coefficient (σ) and flow distortion indices (DC (150) and SC (150)). The DC (150) index is specifically adopted herein because the strong internal–external flow coupling induces a low-energy separation zone with a significant circumferential span at the AIP. Consequently, the wider 150° sector provides a more representative characterisation of the global distortion severity compared to narrower sector definitions (e.g. DC (60)). The metrics are mathematically defined as follows:

Total pressure distortion (DC (150)) evaluates the normalised total pressure deficit between the low-energy region (150° sector) and the main flow at the aerodynamic interface plane AIP, expressed as:

$$DC\,(150) = \frac{\overline{P_{tAIP}} - \overline{P_{t150}}}{0.5\rho_0 {v_0}^2} \tag{4}$$

where $\overline{P_{tAIP}}$ is the mass flow average total pressure at AIP, $\overline{P_{t150}}$ is the average total pressure within the critical 150° sector, $0.5\rho_0 {v_0}^2$ is the freestream reference dynamic pressure before the lip.

https://doi.org/10.1017/aer.2026.10186 Published online by Cambridge University Press

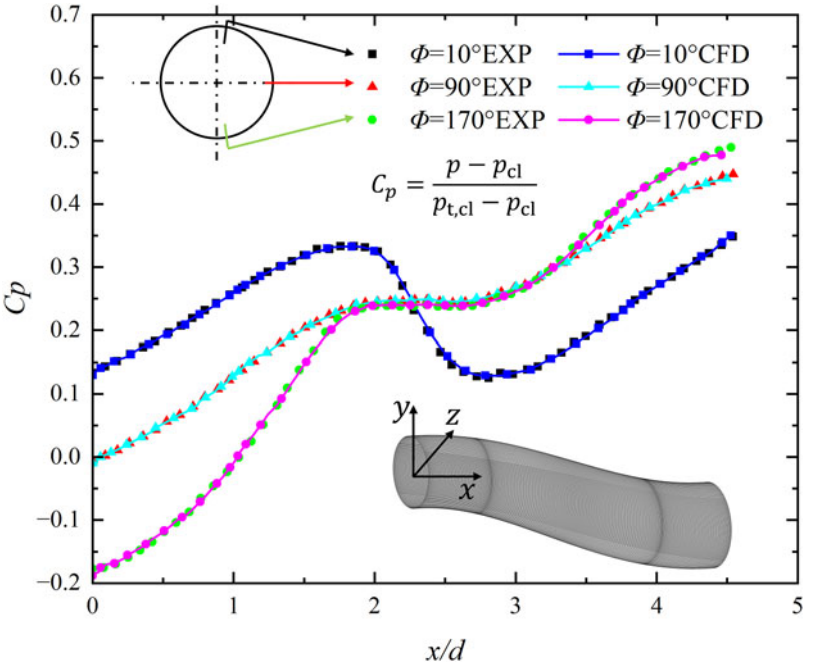


Figure 9. *Comparison of axial distribution of surface static pressures for three circumferential positions.*

Swirl distortion (*SC* (150)) characterises secondary flow intensity through circumferential velocity variations:

$$SC(150) = \frac{v_{CFMAX} - v_{CFMIN}}{\overline{v_{AIP}}} \tag{5}$$

where v_{CFMAX} is the maximum swirl velocity in 150° sector, v_{CFMIN} is the minimum swirl velocity in 150° sector, $\overline{v_{\mathrm{AIP}}}$ is the mass flow average velocity at the AIP.

Total pressure recovery coefficient (σ): the ratio of AIP total pressure ($\overline{P_{\mathrm{tAIP}}}$) to total pressure at intake lip (P_{t1}):

$$\sigma = \frac{\overline{P_{tAIP}}}{P_{t1}} \tag{6}$$

Normalised wall pressure differential (D_P): this parameter serves as an effective indicator of the longitudinal pressure gradient within S-shaped intake ducts, which represents the primary driving mechanism for secondary flow development in such configurations. Consequently, it provides a quantitative basis for assessing the evolution of internal secondary flows:

$$D_P = (P_{upper} - P_{lower})/P_{lower} \tag{7}$$

where P_{upper} and P_{lower} are the static pressure on the upper wall and the lower wall, respectively.

Jet momentum coefficient (C_μ) [30, 31]: The relative momentum flux of control jets:

$$C_\mu = \frac{\dot{m}_j U_j}{0.5 \rho_{AIP} \overline{v_{AIP}}^2 A_{AIP}} \tag{8}$$

where $\dot{m}_j$ denotes the jet mass flow rate, U_{j} represents the jet velocity, while ρ_{AIP} and A_{AIP} correspond to the air density and area at the AIP of the S-intake, respectively.

https://doi.org/10.1017/aer.2026.10186 Published online by Cambridge University Press

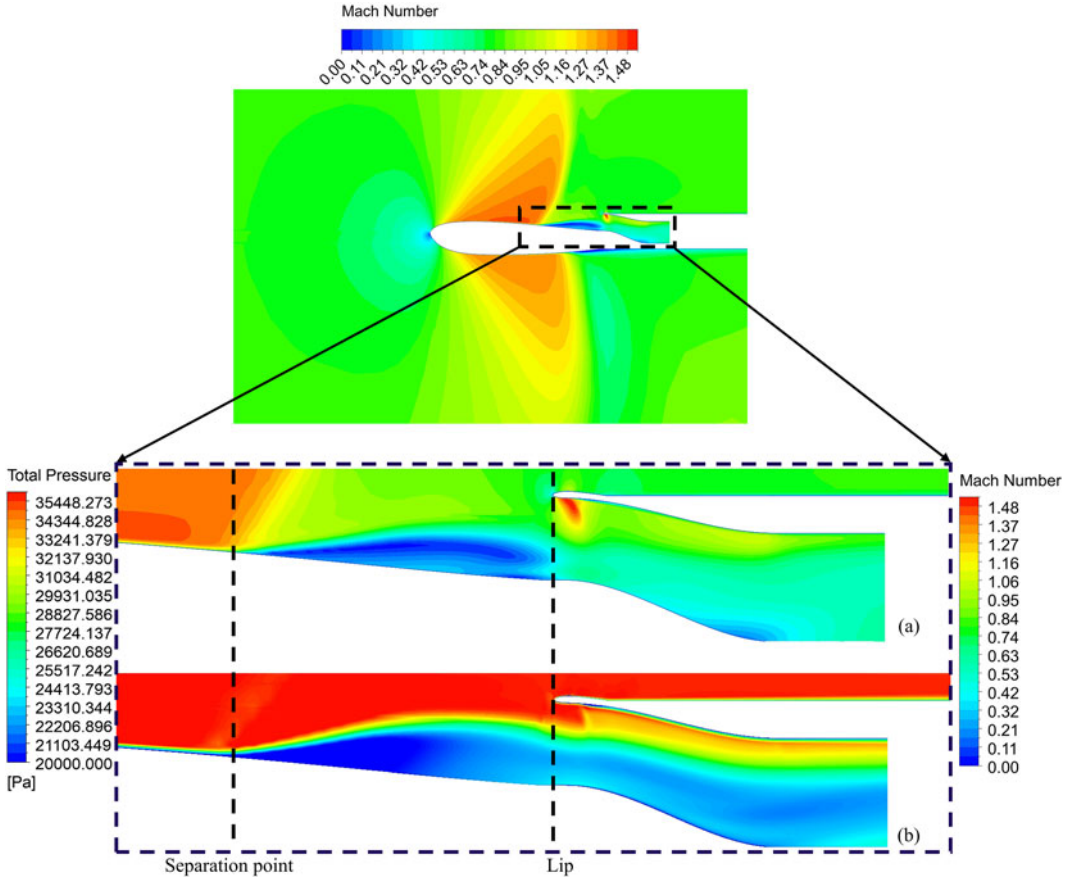


Figure 10. *Global side-view of the flow field and local magnified views of (a) Mach number and (b) total pressure on the meridian plane.*

Power consumption coefficient (P_s): The normalised energy requirement for boundary layer suction:

$$P_s = \frac{\Delta P_{suction} \dot{m}_s}{0.5 \rho_{AIP} \overline{v_{AIP}}^3 A_{AIP}} \tag{9}$$

where $9\Delta P_{suction}$ and $\dot{m}_s$ are the pressure difference acting on the suction process and the suction flow rate, respectively.

3.0 Results and discussions

3.1 Result of wing suction control

3.1.1 Mechanism analysis of single-row distributed suction control

Figure 10 presents total pressure and Mach number contour plots near the wing upper surface upstream of the intake lip. As illustrated in the global side-view of the Mach contour, although the freestream cruise Mach number is 0.85, the convex curvature of the BWB fuselage profile strongly accelerates the incoming flow, causing local regions upstream of the intake to reach supersonic speeds. The local zoomed-in views detailed in Fig. 10 further show the total pressure and Mach number distributions ahead of the lip. Figure 11 shows the static pressure distribution along the wing upper surface meridian. A shock wave under the influence of high flight Mach number and wing surface profile creates a significant adverse pressure gradient (APG) in the flow approaching the intake. Concurrently, intake diffusion

https://doi.org/10.1017/aer.2026.10186 Published online by Cambridge University Press

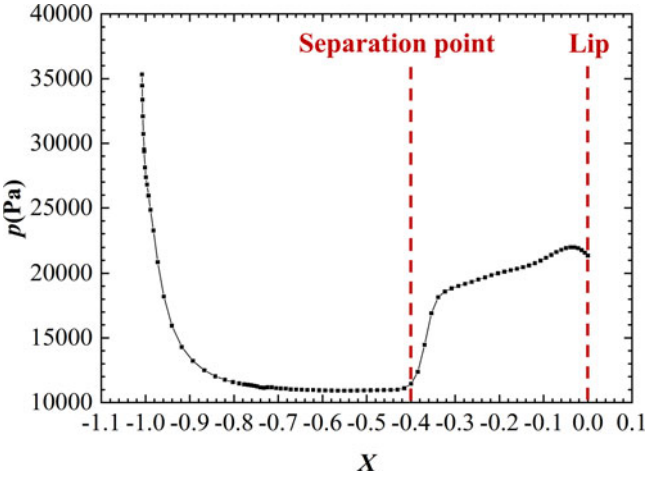


Figure 11. *Static pressure on the upper wing of the meridional plane along the streamwise direction.*

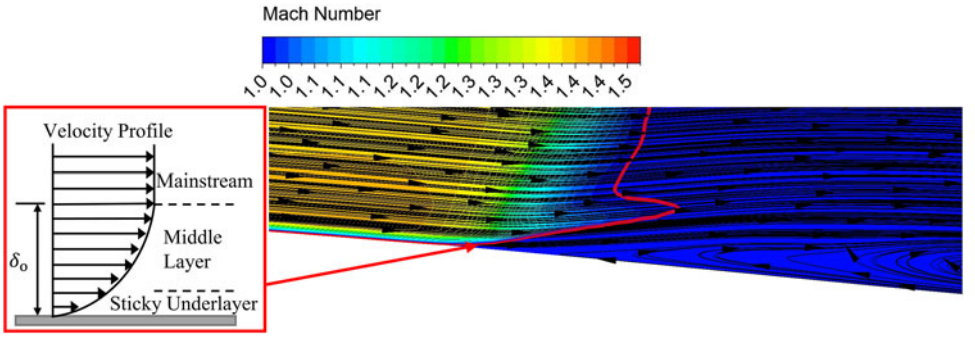


Figure 12. *Upper wing Mach number, streamline and boundary layer diagram.*

and lip blockage exacerbate this pressurisation effect, ultimately leading to the severe flow separation observed immediately downstream of the shock wave in Fig. 10.

According to flow field analysis and references [32, 33], interaction between shock waves and boundary layers (Fig. 12: Mach number contours and streamlines with shockwave highlighted by red lines) causes low-momentum boundary layer fluid to separate under APG. Flow reversal in the boundary layer subsequently obstructs incoming flow, forming a recirculation zone ahead of the lip (Fig. 11). Effective control requires an increase in the momentum of the boundary layer in front of the shock wave to resist the change in flow direction caused by APG. By installing suction tubes on the wing surface, this study enhances wall-boundary layer momentum for external flow control. However, no universal research exists for optimising suction tube placement to achieve control objectives with minimal power consumption. Thus, comparative studies are conducted on suction layouts that minimise suction flow requirements and elucidate mechanisms for performance improvements.

Two distributed single-row configurations – tube *3 and tube *12 arrays (Fig. 13) – are tested, preserving equal total cross-sectional area and comparable mass flow rates (Table 3). Distributed suction tubes are arranged within the spanwise width of the intake's upstream lip region, with their axial positions specifically located at the flow separation point identified in Fig. 10. It should be noted that the suction control in this study is implemented by physically modeling and meshing the actual tube structures on the wing surface, rather than using mathematical source terms in the solver. A prescribed mass flow outlet boundary condition is applied at the bottom end of these meshed tubes to extract the exact suction mass flow.

https://doi.org/10.1017/aer.2026.10186 Published online by Cambridge University Press

Table 3. *Suction tube *3 and *12 parameters*

Parameters	*3	*12
Number	3	12
Side length/D_{out}	0.2	0.05
Span/D_{out}	0.48	0.1
Angle to the wing surface (°)	50	50
Suction flow/Intake flow	1.3%	1.2%

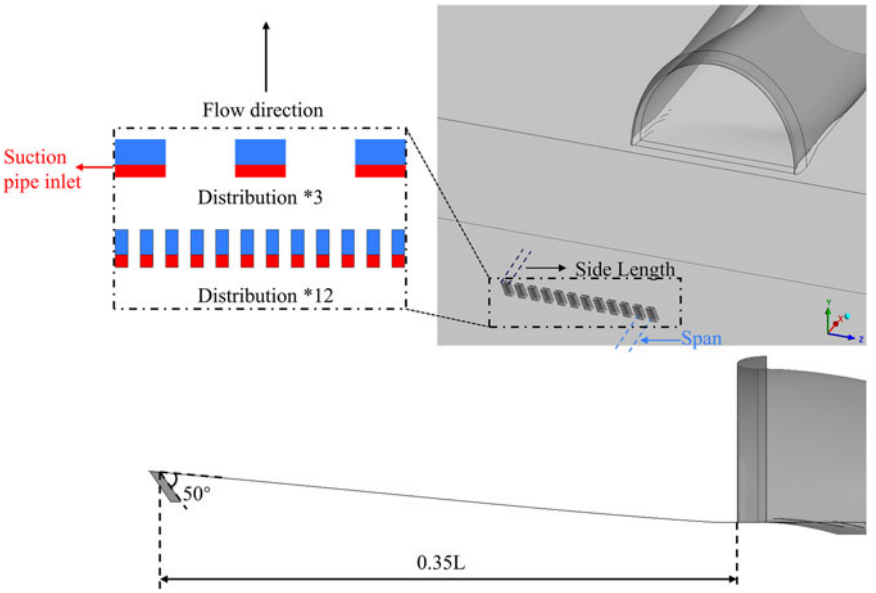


Figure 13. *Location of the suction pipe and the schematic diagram of the two schemes.*

As illustrated in Fig. 14, the suction tubes shift the separation point downstream toward the intake lip and weaken the back flow phenomenon within the separation zone, increasing the average total pressure in the lip boundary layer, resulting in a drastic reduction in the boundary layer thickness ingested by the intake. At the AIP, total pressure magnitude and the high-pressure region area improve significantly. Table 4 compares the AIP total pressure recovery coefficient, demonstrating that both configurations enhance performance, with the 12-tube design showing superior results.

As shown in Fig. 14 and Table 4, the 3-tube suction configuration exhibits a distinct recirculation zone downstream of the suction position and a thicker boundary layer compared to the 12-tube configuration. Additionally, the average total pressure in the AIP's high-pressure region is lower, resulting in significantly reduced flowability. Conversely, the 12-tube configuration demonstrates superior improvement in the AIP's total pressure recovery coefficient. These observations necessitate a comparative study of distributed suction control mechanisms.

Figure 15 illustrates total pressure comparisons on the wing's upper surface at suction tube locations. Significant differences in boundary layer total pressure exist among the three configurations. The suction tubes in both schemes serve to draw in the boundary layer fluid, implying that their differing control effects stem from structural differences. The suction process not only removes the near-wall low-energy fluid, but also creates vortices at the tube inlet, enhancing mixing between the boundary layer gas and the main flow. This introduces high-momentum mainstream gas into the boundary layer. However, differing

https://doi.org/10.1017/aer.2026.10186 Published online by Cambridge University Press

Table 4. *Total pressure recovery coefficient of AIP of no suction and two suction schemes*

	σ	$\Delta\sigma$ (%)	P_s
No control	0.916		
Distribution *3	0.958	4.6	0.0008
Distribution *12	0.963	5.1	0.0005

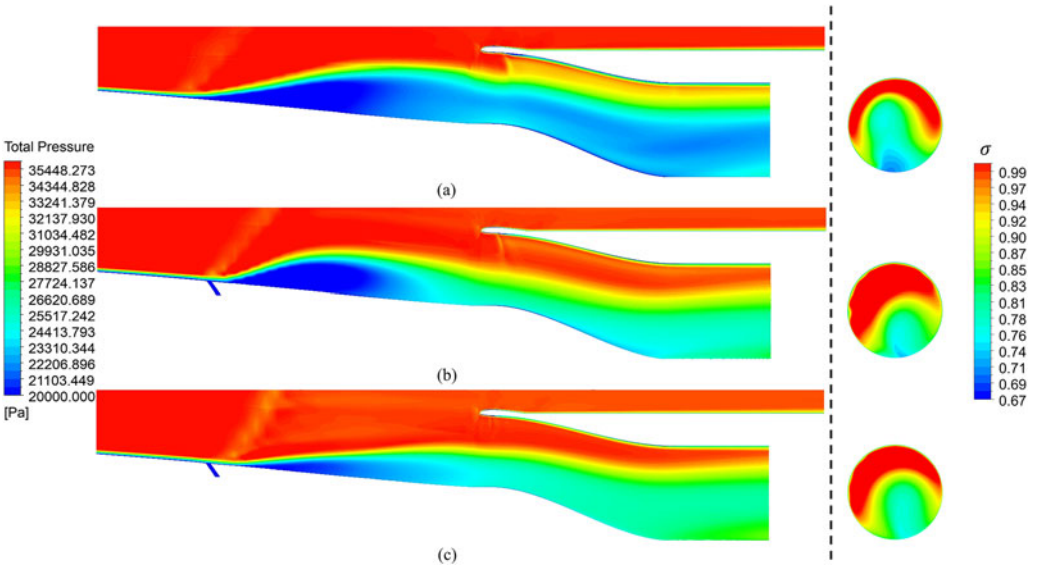


Figure 14. *Total pressure of the meridian plane and σ of AIP: (a) no control, (b) tube *3, (c) tube *12.*

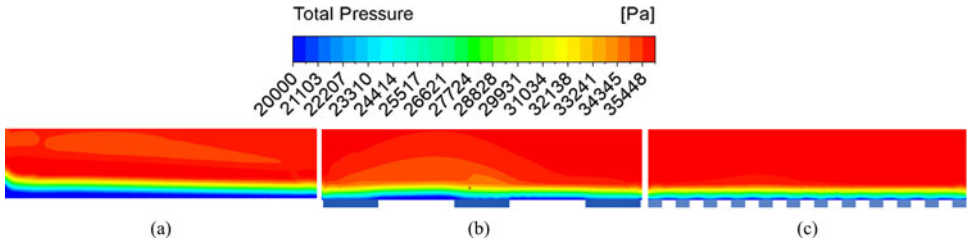


Figure 15. *Near-wall total pressure: (a) nNo control, (b) distribution *3, (c) distribution *12.*

tube spacing produces distinct vorticity distributions, and it is necessary to introduce the near-wall axial vorticity for comparative analysis.

The Q-criterion [34] is employed for flow visualisation to further elucidate the spatial topology of the vortex evolution and the mechanism of separation suppression, where Q > 0 indicates the dominance of rotational motion. Figure 16 presents the iso-surfaces ($Q = 1 \times 10^4 s^{-2}$) near the suction region for the baseline and controlled cases.

In the uncontrolled case (Fig. 16(a)), large-scale irregular vortex structures are observed hovering above the wing surface, corresponding to the massive separation zone induced by the shock wave. With suction control applied, regular vortex structures are generated in the near-wall region of the suction tube orifices. The mixing effect caused by these induced vortices promotes the breaking and decomposition of the large-scale separation vortex structure in the separation zone. Comparing the two suction schemes,

https://doi.org/10.1017/aer.2026.10186 Published online by Cambridge University Press

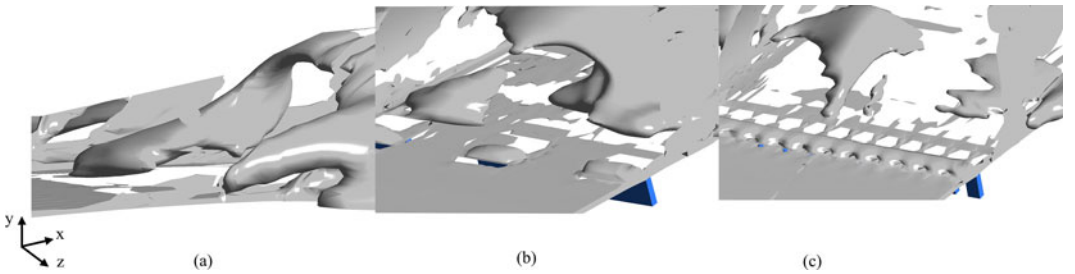


Figure 16. *Iso-surfaces of Q-criterion* ($Q = 1 \times 10^4 s^{-2}$) *near the suction region: (a) no control, (b) distribution *3, (c) distribution *12.*

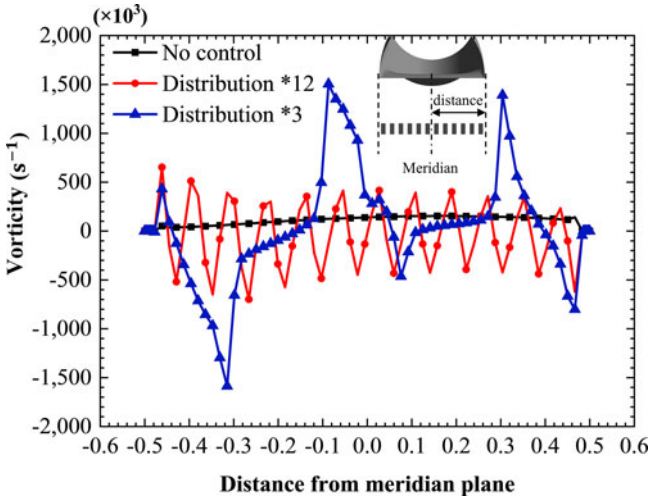


Figure 17. *Vorticity distribution along the spanwise direction near the suction pipe on the upper wing surface.*

the 12-tube configuration (Fig. 16(c)), with its tighter spanwise spacing, exhibits a stronger capability to break down large-scale vortices than the 3-tube scheme (Fig.16(b)). This intensified interaction effectively prevents the re-coalescence of large eddies, thereby significantly improving the downstream separation status.

Figure 17 depicts axial vorticity distributions within the suction region on the wing's upper surface. The horizontal coordinate represents normalised distance from the meridional plane, while the vertical coordinate shows axial vorticity magnitude. Without control, the spanwise axial vorticity distribution is weak with no significant swirling structures. The 3-tube configuration exhibits higher peak axial vorticity, but it remains confined near suction locations with no interconnections and uneven magnitude distribution. In contrast, the 12-tube configuration displays multiple uniformly distributed vorticity pairs along the spanwise direction. This indicates that the mechanism of suction control is to produce multiple pairs of uniform vortex structures on the upper surfaces of the wings while sucking the boundary layer.

As illustrated in Fig. 18, the detailed mechanism of suction-induced mixing is visualised. The coloured arrows along the streamwise direction represent the velocity vectors in the near-wall region. It is observed that the velocity magnitude remains relatively high with minimal decay directly above the suction port inlet (indicated by the blue tube region), whereas the velocity vectors on both lateral sides exhibit a drastic deceleration as they approach the wall. Furthermore, the spanwise slices across the suction tubes display vorticity iso-surfaces overlaid with black streamlines. These flow patterns reveal that the specific vorticity structures near the suction tubes drive the high-energy mainstream fluid from the lateral sides to converge toward the centre. This convective transport energises the local flow, resulting

https://doi.org/10.1017/aer.2026.10186 Published online by Cambridge University Press

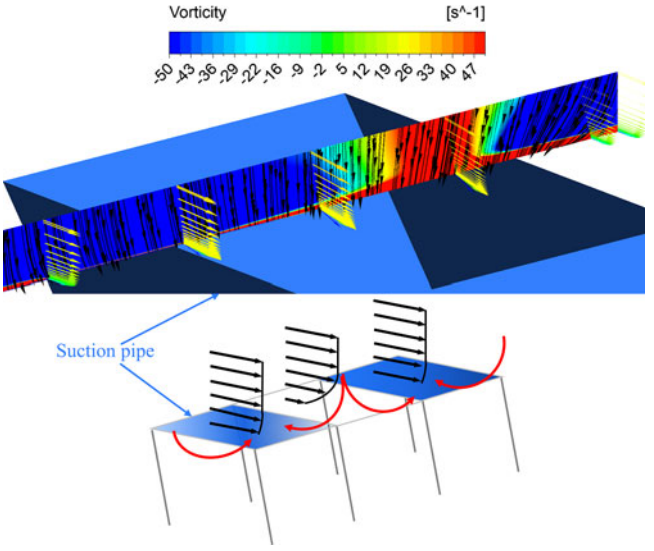


Figure 18. *Schematic diagram of suction-induced mixing flow.*

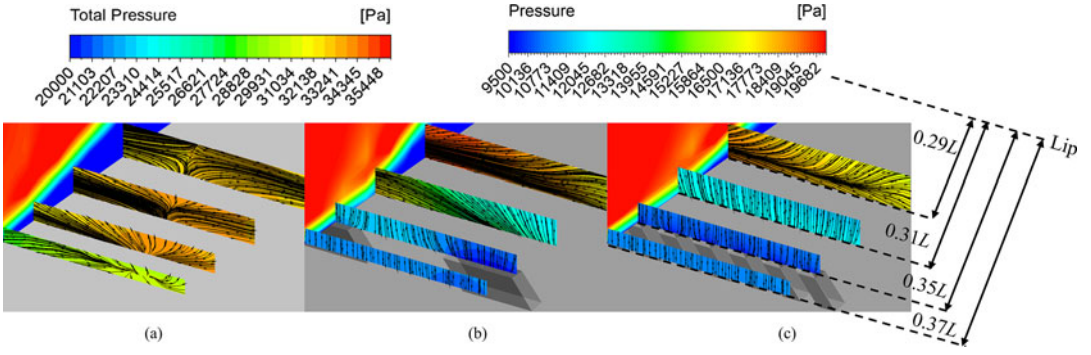


Figure 19. *Near-wall streamline, static pressure and total pressure distribution on the meridian plane of no suction and two suction schemes: (a) no control, (b) distribution* *3, (c) distribution* *12 (contour slices on the meridian plane represent total pressure, while spanwise slices along the suction tubes depict static pressure).*

in a fuller boundary layer profile at the suction port interface (as schematically depicted at the bottom of the figure). Consequently, this secondary flow effectively introduces high-energy mainstream fluid into the boundary layer, increasing its saturation (kinetic energy fullness). However, maintaining this beneficial structure requires a balance between the induced secondary flows and the mainstream flow to prevent excessive blockage.

Figure 19 reveals the wall streamline and static pressure development. It can be seen that when the spacing is too large (such as 3-tube case), the intensity of a single suction vortex is too high, which disrupts the continuity of the boundary layer. Near-wall static pressure increases significantly, and soon the near-wall streamlines downstream of the suction tube turn towards the wing spanwise direction. When the spacing is moderate (such as 12-tube case), the vortex array is more stable, achieving better momentum mixing. At the same downstream position, the streamline remains normal to the wing surface, indicating that momentum continues to transfer from the mainstream to the boundary layer. Consequently, boundary layer thickening occurs further downstream, enhancing suppression of the downstream boundary layer.

https://doi.org/10.1017/aer.2026.10186 Published online by Cambridge University Press

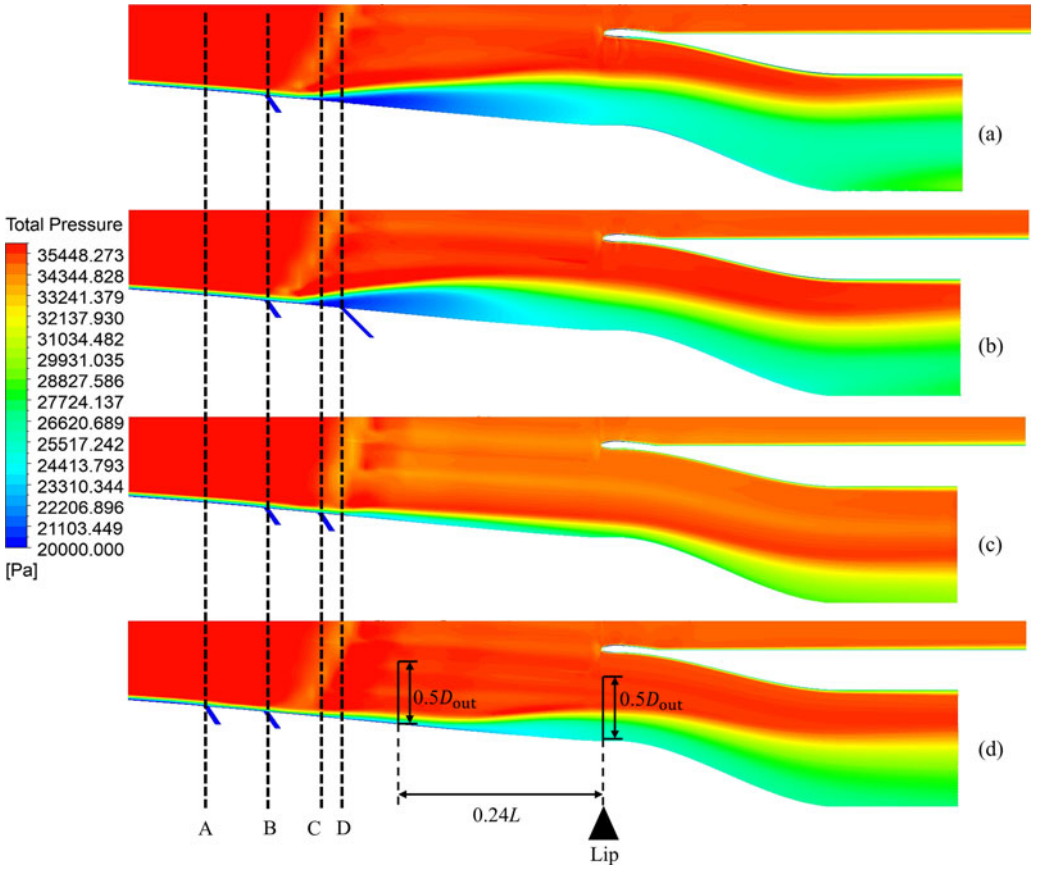


Figure 20. *Total pressure on the meridian plane for four suction tube arrangements: (a) single-row suction; (b) suction at positions B and D; (c) suction at positions B and C; (d) suction at positions A and B.*

3.1.2 Mechanism analysis of different double row suction positions

Through the research in 3.1.1, it is observed that the addition of suction tubes can cause the separation point to move. In actual flight, the separation point also shifts due to varying operational conditions. This study designed a second row of suction tubes to address this issue, aiming to broaden the range of operational conditions where suction control is effective and to optimise control performance. In addition to the existing single-row suction position B, the suction tubes are also placed at positions A (in front of the single-row suction tubes), C (near the shock wave close to the new separation point under single-row suction conditions) and D (behind the shock wave under single-row suction conditions) to analyse the effects of double-row suction.

Figure 20 presents the positions of the suction tubes and the total pressure comparison on the meridian plane for four different cases. Figure 21 shows the Mach number comparison on the meridian plane for four different cases. Figure 22 illustrates the static pressure distribution along the centreline of the upper surface of the wing. It can be seen that the suction effect can accelerate the local near-wall flow. Compared with single-row suction and no suction, the outlet pressure of double-row suction increases under the same flow rate, and the flow capacity is significantly improved.

Dual-row suction demonstrates superior boundary layer thickness control at the intake, reducing ingested thickness while eliminating the supersonic region and associated shock wave losses. The AB and BC configurations achieve the most significant improvements, and the intake boundary layer thickness can be reduced to less than 50%. Their notable feature is the placement of suction tubes at or

https://doi.org/10.1017/aer.2026.10186 Published online by Cambridge University Press

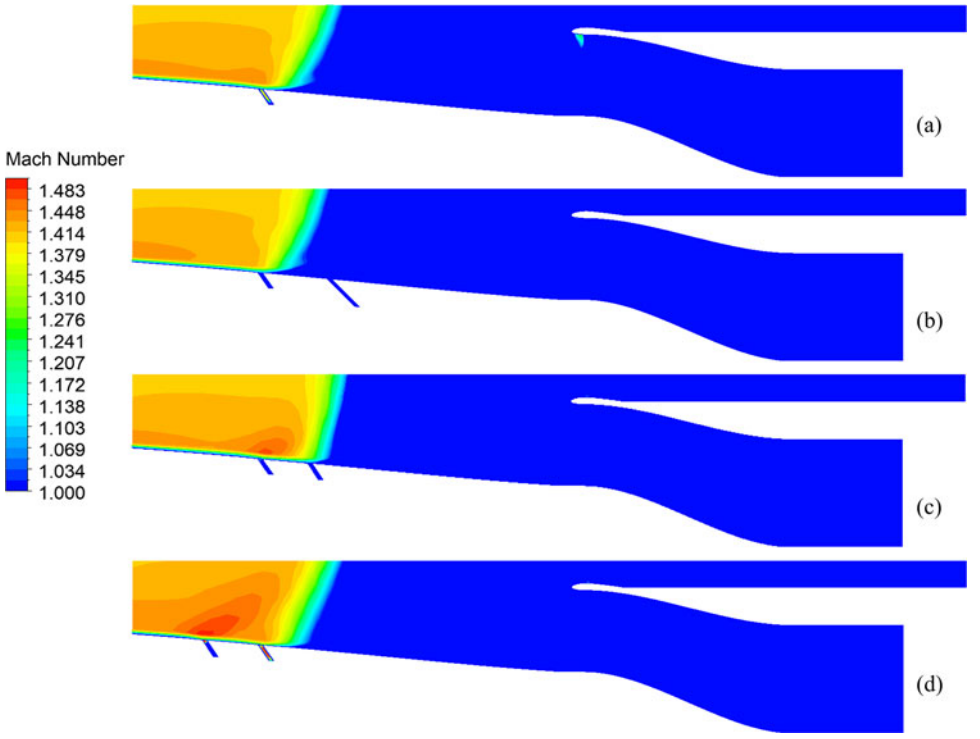


Figure 21. *Mach number on the meridian plane for four suction tube arrangements: (a) single-row suction; (b) suction at positions B and D; (c) suction at positions B and C; (d) suction at positions A and B.*

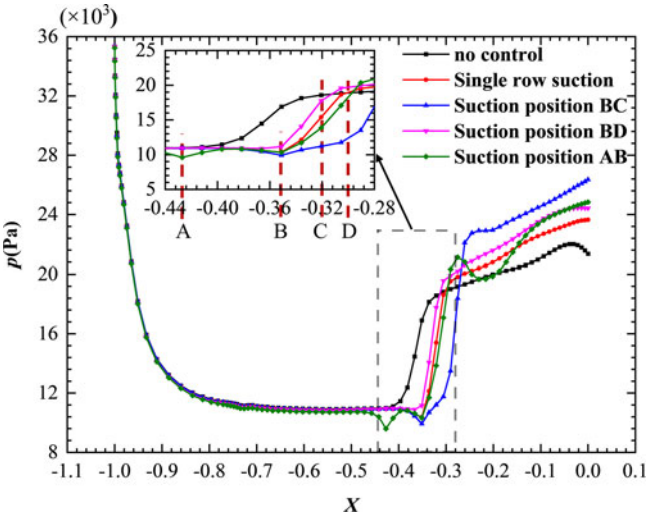


Figure 22. *Static pressure along the flow direction on the centreline of the upper wing surface.*

upstream of the shock wave, enabling the near-wall fluid to maintain greater kinetic energy to resist the APG passing through the shock wave. In contrast, when BD is arranged, the suction pipe at position D is located behind the shock wave, and the separation has already been initiated, so its participation in control is limited. Overall, the control effect is not much different from that of single-row suction (Fig. 23).

https://doi.org/10.1017/aer.2026.10186 Published online by Cambridge University Press

Table 5. *AIP parameters and suction power*

	σ	$\Delta\sigma$(%)	P_s
No control	0.916		
Single row suction	0.963	5.1	0.0005
Suction position BD	0.978	6.8	0.0021
Suction position BC	0.993	8.4	0.0018
Suction position AB	0.987	7.8	0.0013

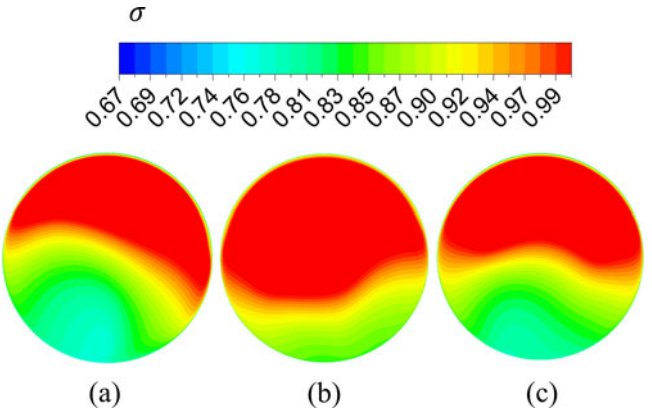


Figure 23. *σ of AIP: (a) suction position BD, (b) suction position BC, (c) suction position AB.*

Table 5 presents the total pressure recovery coefficient (σ) and consumed power (P_s) for single-row and three dual-row configurations, where $\Delta\sigma$ denotes the relative difference between controlled and uncontrolled total pressure recovery coefficients. Energy analysis reveals suction consumes less than 0.3% of intake kinetic energy while delivering at least 5% improvement in total pressure recovery coefficient. Among dual-row configurations, the BC positioning achieves the maximum recovery coefficient gain (8.4%) with relatively low power consumption.

When the total pressure recovery coefficient serves as the evaluation metric, the BC configuration demonstrates optimal performance. The single-row and BD arrangements exhibit comparable effectiveness, while the AB layout yields intermediate results. The near-wall velocity distribution is extracted from the intake lip and the upstream $0.24L$ as shown in Fig. 24. The height from the wall is $0.5D_{out}$. The dimensionless results are shown in Fig. 24 (where U_e is the mainstream streamwise velocity). By combining the meridian plane total pressure contours, it can be found that the AB and BC configurations have fuller velocity profiles at the lip and upstream positions, with significantly reduced boundary layer thickness. These arrangements effectively suppress recirculation zones downstream of suction tubes. However, the suction position of the AB layout is relatively far from the intake, and this control effect cannot be well maintained. As a result, the velocity profile of the AB layout at the lip is closer to that of the less effective BD layout, and a thicker boundary layer is re-accumulated.

Section 3.1.1 indicates that the primary aerodynamic effect of the suction on the wing surface arises from the mixing induced by interactions between counter-rotating vortex pairs. In the previous part of the discussion in this Section 3.1.2, the dual-row suction tubes maintain the spanwise-aligned positioning in one-to-one correspondence. This configuration amplifies vorticity mixing from leading-row tubes, enhancing flow control efficacy. However, spanwise-staggered arrangement of the second-row tubes relative to the first may intensify three-dimensional mixing and improve boundary layer kinetic energy replenishment, but may also disrupt symmetrical vortex pairs, leading to uneven mixing and possibly causing unexpected secondary swirl. The following analysis employs the BC configuration.

https://doi.org/10.1017/aer.2026.10186 Published online by Cambridge University Press

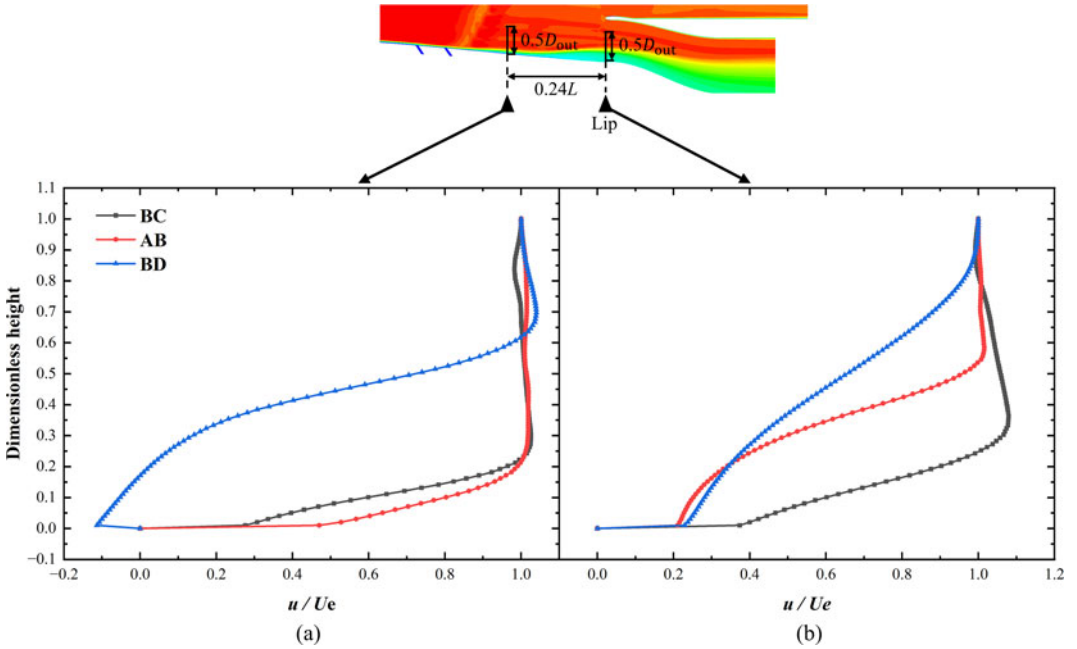


Figure 24. *Near-wall velocity distribution: (a) 0.24L upstream of the lip, (b) at the lip.*

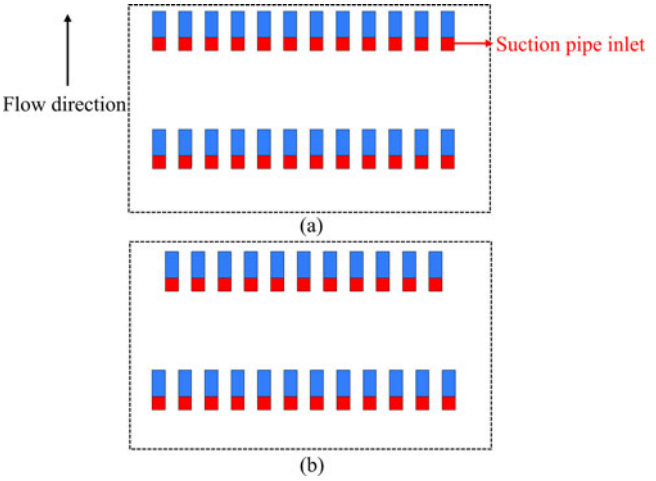


Figure 25. *Schematic diagram of suction pipe: (a) parallel distribution, (b) staggered distribution.*

Figure 25 illustrates parallel versus staggered arrangements, indicating that the second-row tubes are laterally shifted relative to the first row.

Figure 26 compares total pressure distributions on the meridian plane and AIP section for parallel and staggered configurations. Relative to parallel distribution, the staggered arrangement exhibits intensified flow separation downstream of the second suction row, reduced near-wall total pressure and expanded low-pressure regions at the AIP, decreasing the total pressure recovery coefficient from $\sigma = 0.993$ to $\sigma = 0.979$ ($\Delta\sigma = 0.014$). Figure 27 reveals that in staggered configurations, recirculation zones initiate further upstream and closer to the meridian plane. Meanwhile, the flow near the meridional plane is not as smooth as that in the parallel distribution. This indicates that the second-row suction tubes have a weak or even no mixing effect, as mentioned earlier.

https://doi.org/10.1017/aer.2026.10186 Published online by Cambridge University Press

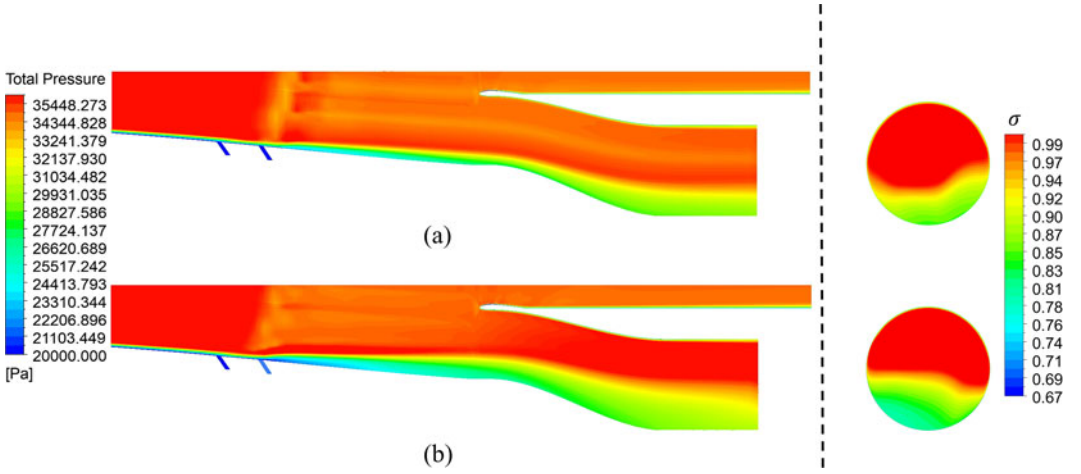


Figure 26. *Total pressure of the meridian plane and σ of AIP section: (a) parallel distribution, (b) staggered distribution.*

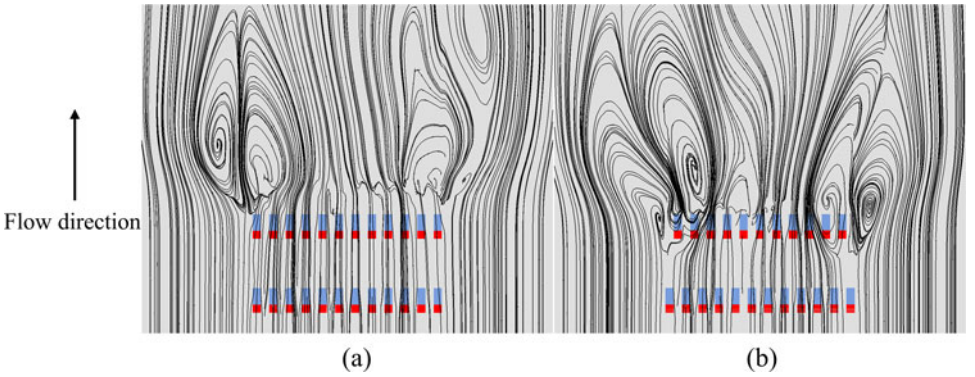


Figure 27. *Wing surface streamline: (a) parallel distribution, (b) staggered distribution.*

Figure 28 demonstrates significant axial velocity reduction downstream of the first suction row in staggered arrangements due to spanwise misalignment. This accelerated transverse flow diminishes resistance to adverse pressure gradients compared to parallel configurations.

The impact of the arrangement on the vortex topology evolution is further visualised using Q-criterion iso-surfaces in Fig. 29. As the airflow passes through the first row of suction tubes, regular small-scale vortex structures are generated in the near-wall region for both configurations. However, significant distinct behaviours emerge as the flow encounters the second row.

In the parallel distribution (Fig. 29(a)), the vortices generated by the second row constructively inherit the flow structures from the first row, maintaining the stream-wise continuity of the vortex pairs and further suppressing the formation of large-scale separation bubbles downstream. Conversely, in the staggered distribution (Fig. 29(b)), the second row of suction tubes disrupts this beneficial interaction to a certain extent. The spanwise misalignment interrupts the established vortex path, leading to the re-emergence of large, irregular vortex structures detaching from the wall in the downstream region, which effectively exacerbates the separation as indicated by the velocity deficit analysis.

As can be seen from Fig. 30, although staggered arrangements maintain spanwise counter-rotating vortices (with higher lateral vorticity magnitudes), their non-uniform scaling and structural incompatibility disrupt first-row symmetric vortical structures. Consequently, near-wall streamlines at the

https://doi.org/10.1017/aer.2026.10186 Published online by Cambridge University Press

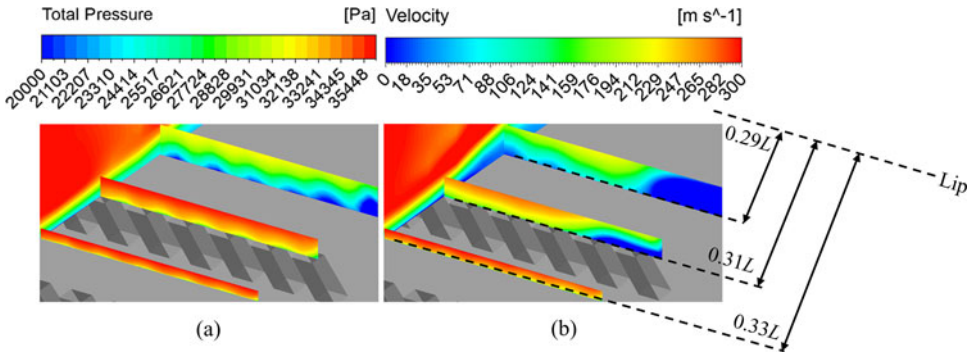


Figure 28. *The axial velocity near the wall before and after the second row of the suction pipe and the total pressure on the meridian plane: (a) parallel distribution, (b) staggered distribution (contour slices on the meridian plane represent total pressure, while spanwise slices along the suction tubes depict axial velocity).*

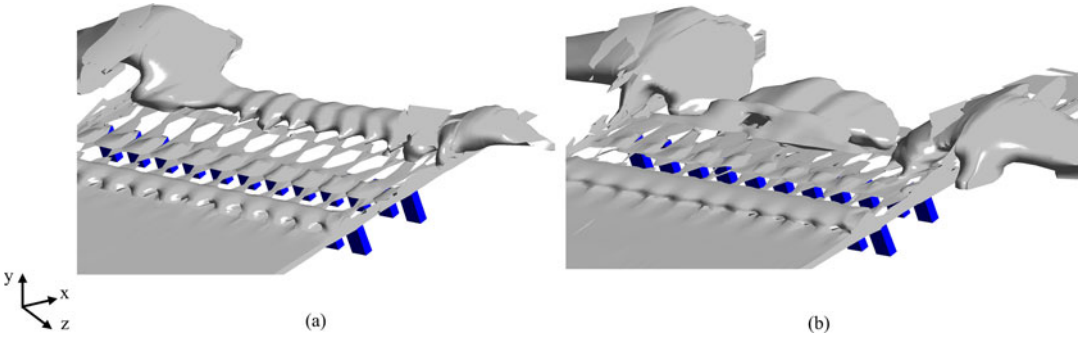


Figure 29. *Comparison of Q-criterion iso-surfaces ($Q = 1 \times 10^4 s^{-2}$) for dual-row suction strategies: (a) parallel distribution, (b) staggered distribution.*

second-row deviate from wall-normal directions (Fig. 31), causing non-uniform mixing and elevated adverse pressure gradients downstream.

3.2 Result of combined control of wing suction and intake jet flow

3.2.1 Scheme of wing suction and intake jet combination

Although external suction improves intake recovery, it cannot address the secondary swirl and total pressure distortion developing inside the duct. To overcome this limitation, building upon the outflow optimal control scheme (parallel distributed suction tubes at the BC location) presented in Section 3.1.2, this section introduces internal jet injection to form a coupled control system designed to augment external suction benefits and optimise internal flow quality. Figure 32 depicts the intake duct and jet tube configuration, and the jet tubes' geometry is shown in Table 6. The jet tubes are arranged at the first bend of the intake, which is the separation point within the intake during suction control.

It should be noted that the jet tubes are oriented at a pitch angle of 20° (i.e. the angle with the local tangent plane of the lower wall surface, injecting downstream). Similar to the suction setup described previously, the jet control is realised by explicitly generating grids for the physical jet pipes, rather than using mathematical source terms. A prescribed mass flow inlet boundary condition is assigned at the entrance of these pipes to inject fluid.

https://doi.org/10.1017/aer.2026.10186 Published online by Cambridge University Press

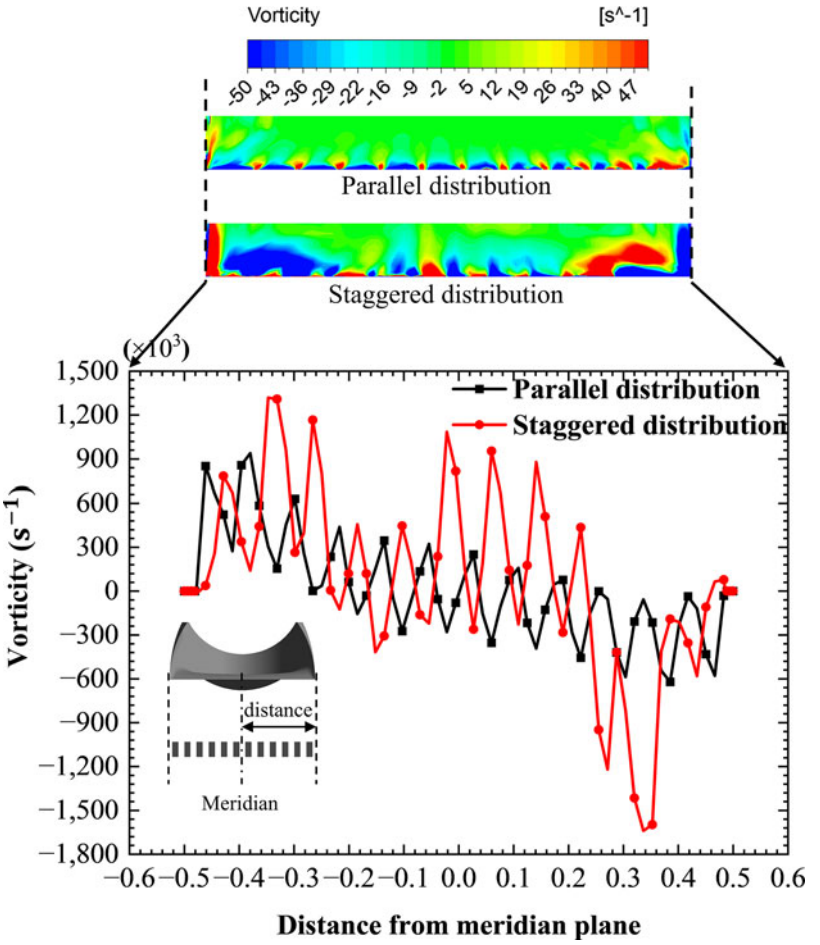


Figure 30. *The vorticity distribution along the spanwise direction of the wall at the second row of suction pipe.*

3.2.2 Analysis of partition jet control mechanism

Figure 33 [35] schematically depicts the generation of secondary swirl flow in the curved duct. The low-energy fluid mass at the intake outlet originates primarily from two sources: (1) flow separation due to adverse pressure gradients along the lower wall and (2) fluid cross-migration (secondary swirl) induced by centrifugal forces at the first bend and pressure gradients from differentials between sidewalls and the meridian plane. Consequently, the jet region can be divided into three zones, A, B and C, as shown in Fig. 34, which are just able to correspond to the zones where the above two types of losses occur. Zone B losses derive predominantly from the first source, while secondary flow losses result from synergistic interactions between lateral zones A/C and zone B. Building on this division, this research proposes a partitioned jet control strategy. The mechanisms governing partition jet influence are analysed subsequently.

The initial investigation examines control mechanisms in the lateral AC zones. Two jet schemes are defined for comparative analysis: Scheme I (AC zones: 0.7% total flow, B zone: 0.6%) and Scheme II (AC zones: 1.3%, B zone: 0.6%), with percentages relative to intake flow rate.

Figure 35 compares AIP total pressure distributions for both schemes against baseline. Scheme II reduces the lower-wall low-pressure zone while generating high-pressure regions that disrupt low-energy fluid clusters, fragmenting the low-pressure domain. Table 7 quantifies a 1% decrease in total pressure

https://doi.org/10.1017/aer.2026.10186 Published online by Cambridge University Press

Table 6. *Parameters of jet pipe*

Parameters	Value
Number	15
Side length/D_{out}	0.02
Span/D_{out}	0.03
jet angle (°)	20

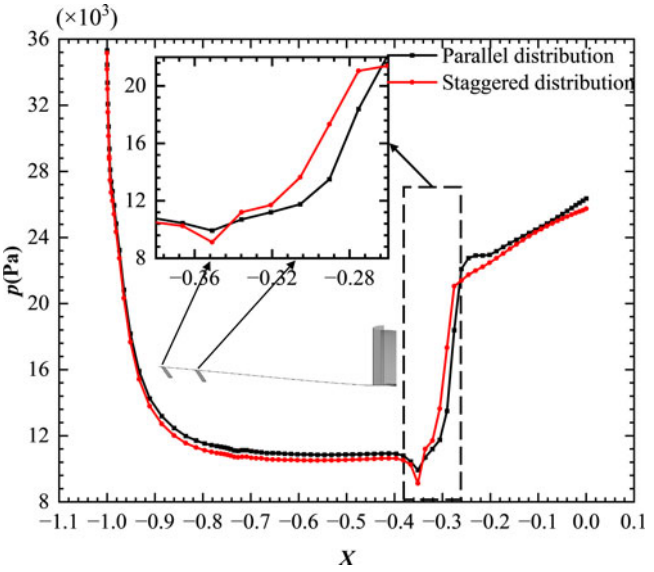


Figure 31. *Static pressure along the flow direction on the centreline of the upper wing surface.*

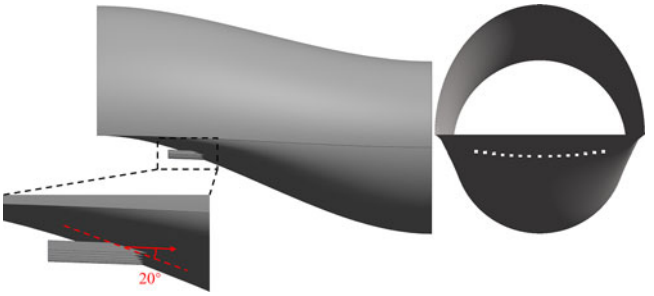


Figure 32. *Coupling structure of intake and jet pipe.*

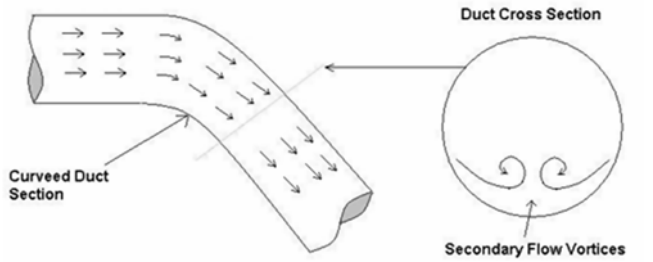


Figure 33. *Secondary swirl in the curved section [35].*

https://doi.org/10.1017/aer.2026.10186 Published online by Cambridge University Press

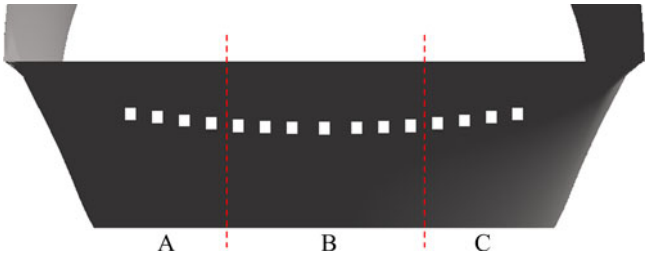


Figure 34. *Jet region division.*

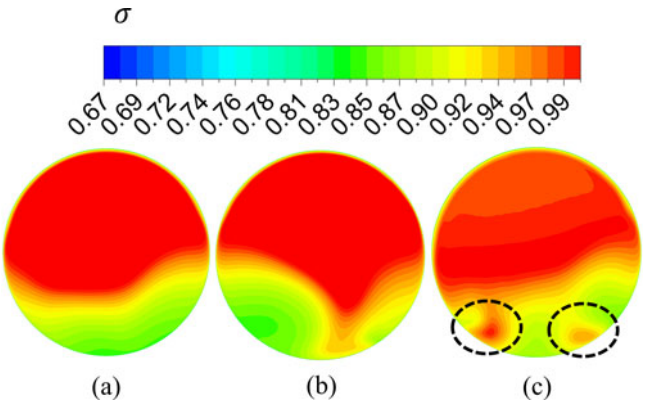


Figure 35. *σ of AIP: (a) baseline, (b) scheme I, (c) Scheme II.*

recovery coefficient but significant improvements: 23% reduction in total pressure distortion and 4.6% decrease in swirl distortion.

The dimensionless differential pressure distribution along the upper and lower wall surfaces is shown in Fig. 36, which is the driving source of the secondary flow in the S-shaped intake, with the abscissa taking the intake start position as the origin and dimensionless by intake length. Scheme I exhibits greater post-first-bend pressure differentials than the no-jet baseline, intensifying secondary flow development. Conversely, Scheme II reduces this differential relative to uncontrolled conditions, correlating with decreased outlet distortion.

Streamline visualisation of Scheme II's AC and B zones (Fig. 37) reveals that in the B zone, only a minor fraction of ingested fluid attaches laterally to walls, while the majority energises separation zones near the central meridian plane, confirming primary action against the first loss mechanism. For the AC zone, in addition to the above effects, fluid integrates into vortex structures through pressure differentials between sidewalls and the meridian plane. This enhances mixing between wall-bounded and mainstream flows, suppressing bilateral lower-wall separation, reducing total pressure distortion and mitigating losses during wing suction control. The AC jet fluid disrupts pre-existing secondary flow by introducing high kinetic energy while intensifying mixing, thereby effectively controlling the second loss.

Scheme III is implemented with increased flow rates to further analyse B-zone jet control mechanisms: B zone 1.1% and AC zone 1.3%. Table 8 quantifies momentum consumption for total pressure recovery coefficient and distortion improvements under different flow conditions, with $\Delta\sigma$, ΔDC (150), ΔSC (150) referenced to Scheme I. The momentum coefficient increased from Scheme I to II primarily results from AC zone flow augmentation, yielding substantial reductions in total pressure distortion and swirl distortion. Conversely, the increase from Scheme II to III originates from B zone flow increase, significantly improving pressure recovery coefficient with negligible swirl distortion change.

https://doi.org/10.1017/aer.2026.10186 Published online by Cambridge University Press

Table 7. *AIP parameters*

	σ	DC(150)	SC(150)
Baseline	0.993	0.203	0.153
I	0.976	0.238	0.175
II	0.980	0.156	0.146

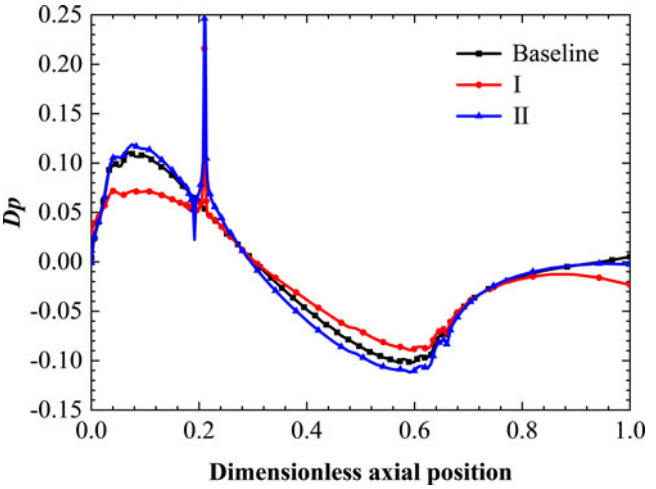


Figure 36. *Static pressure difference of the upper and lower wall along the intake.*

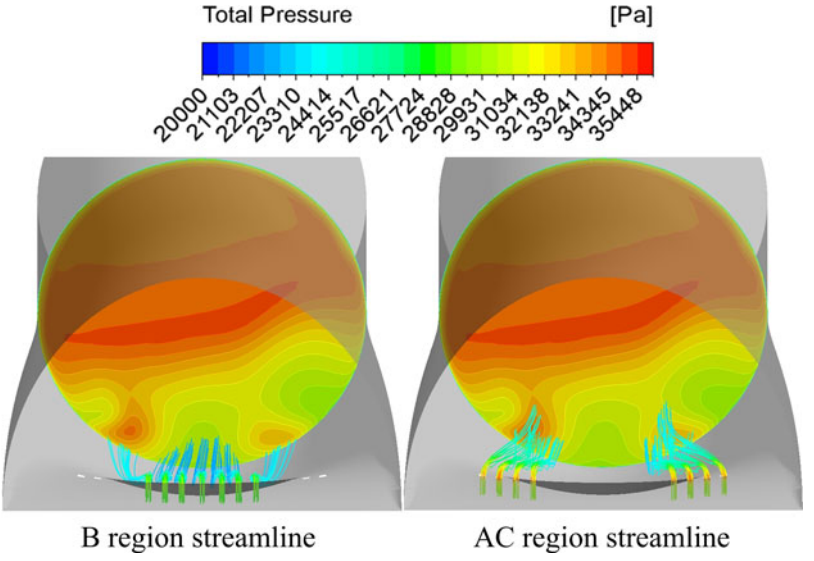


Figure 37. *The streamline from the AC and B region.*

This demonstrates that jet control requires the introduction of momentum ingestion in the appropriate region so as to achieve the best flow field improvement at the lowest possible cost.

The mechanism of the jet control in zone B can be analysed in combination with the total pressure distributions and streamline diagrams of the meridional plane of the intake and the AIP section, as shown in Fig. 38. Increasing the flow ratio in zone B from 0.6% to 1.1% elevates total pressure in lower-wall fluid adjacent to the meridional plane while significantly suppressing central-region separation. AIP concurrently show outward migration of bilateral vortex pairs with higher central-jet flow rates.

https://doi.org/10.1017/aer.2026.10186 Published online by Cambridge University Press

Table 8. *Comparison of energy consumption and benefits of three jet schemes*

	AC flow/ Intake flow (%)	B flow/ Intake flow (%)	C_μ	σ	DC (150)	SC (150)	$\Delta\sigma$(%)	ΔDC (150)(%)	ΔSC (150)(%)
I	0.7	0.6	0.034	0.976	0.238	0.175			
II	1.3	0.6	0.076	0.980	0.156	0.146	0.4	−34.5	−16.6
III	1.3	1.1	0.089	0.992	0.13	0.142	1.6	−45.4	−18.9

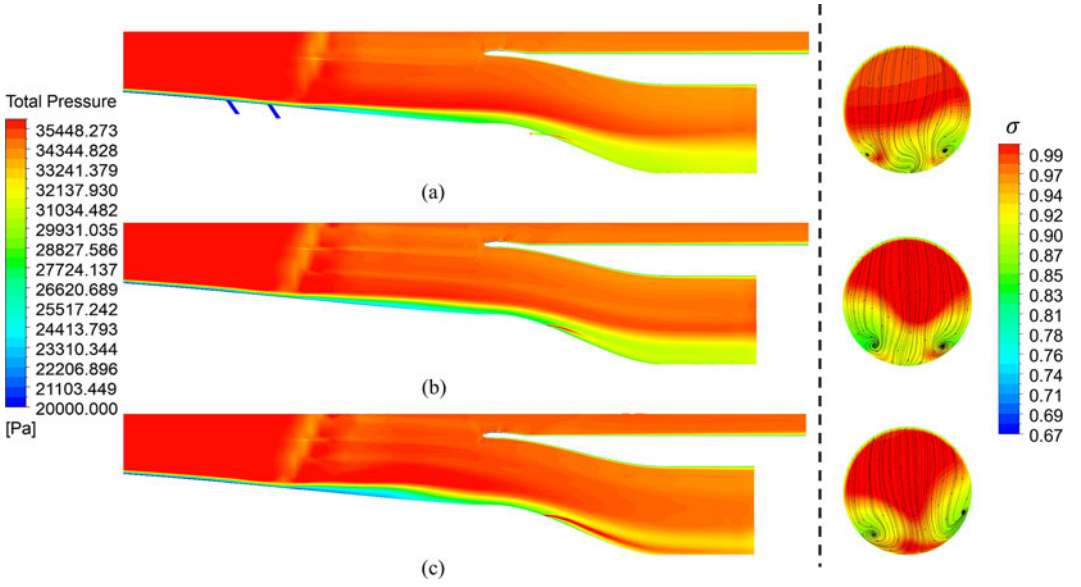


Figure 38. *The total pressure of the meridian plane and σ of AIP under different jet flow rates in region B: (a) 0.6% jet, (b) 0.8% jet, (c) 1.1% jet.*

Figure 39 presents the total pressure distribution along the meridian at $0.4D_{out}$ upstream of the AIP section. The x-axis represents the ratio of the local total pressure on the meridian to the total pressure in the mainstream area of the section, and the y-axis represents the ratio of the local coordinate value to the total height of the section. This cross-section is located downstream of the first bend and the jet gas in the central area is basically in a wall-adhering flow state, which can reflect the effect of energy replenishment in the central area. The 1.1% jet case exhibits universally higher total pressure than other cases, while the 0.8% jet exceeds the 0.6% jet in most regions, confirming significant energy supplementation efficacy.

B-zone jets primarily energise separation zones near the meridian plane, significantly enhancing AIP total pressure recovery coefficient as quantified in Fig. 40.

3.3 Energy benefit analysis

An energy benefit analysis was performed to assess engineering feasibility and balance the aerodynamic gains against the power consumption of the flow control system. Based on the suction power coefficient (P_s) and jet momentum coefficient (C_μ) defined previously, the total power consumption coefficient, C_{P_total}, for the coupled control is defined as:

$$C_{P_total} = P_s + P_j \tag{10}$$

https://doi.org/10.1017/aer.2026.10186 Published online by Cambridge University Press

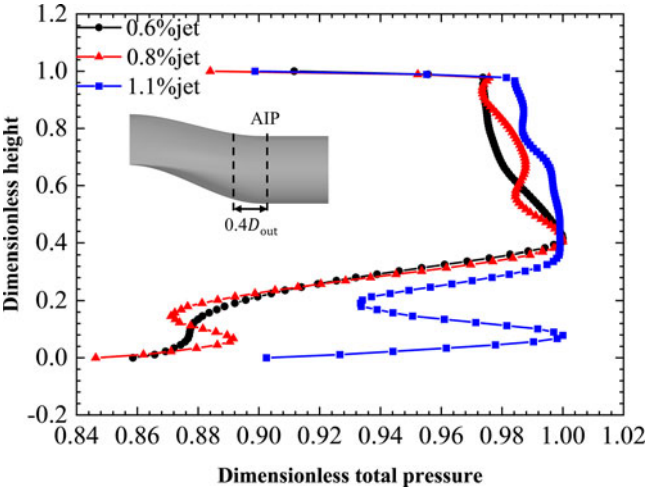


Figure 39. *The total pressure distribution along the height of the second bend under different jet flow rates in region B.*

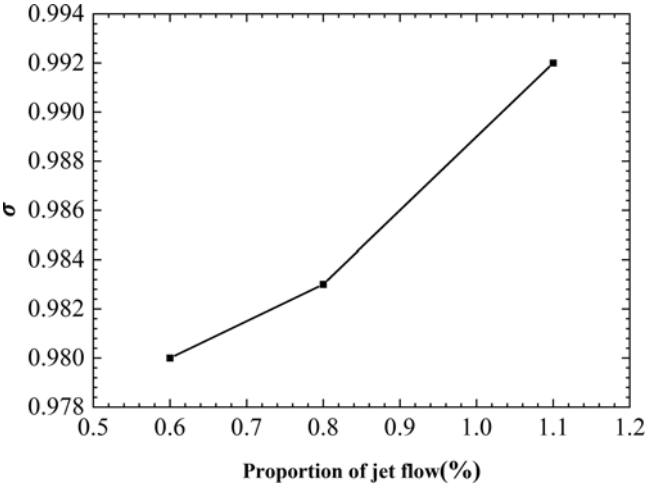


Figure 40. *The total pressure recovery coefficient of AIP at different jet flow rates in region B.*

$$P_j = \frac{0.5\dot{m}_j U_j^2}{0.5\rho_{AIP}\overline{v_{AIP}}^3 A_{AIP}} = \frac{1}{2}C_\mu \cdot \frac{U_j}{\overline{v_{AIP}}} \tag{11}$$

where P_j represents the jet power coefficient, and all other variables are consistent with the definitions in Section 2.4.

For the benefit assessment, the thrust generated by the intake serves as the reference metric. The analysis focuses on the configuration with the highest energy expenditure to provide a conservative estimate. Specifically, this corresponds to the dual-row suction at position BC combined with Jet Scheme III, which demonstrated superior flow control effectiveness. Table 9 presents the comparison between the thrust increment and total energy consumption for this configuration.

The results indicate that while the control strategy incurs an energy penalty equivalent to 7.4% of the mainstream energy, it delivers a substantial 55.5% increase in intake thrust compared to the baseline. Moreover, as previously discussed, this configuration reduces total pressure distortion by 45.4% and

https://doi.org/10.1017/aer.2026.10186 Published online by Cambridge University Press

Table 9. *Comparison of thrust lift and energy consumption*

	Thrust (N)	C_{P_total}
No control	3871.64	
Suction + Jet	6021.52	0.074
Variation	55.5%	7.4%

swirl distortion by 18.9%, providing a critical safety margin for the compressor. These findings validate that the energy expenditure is well-justified by the performance improvements.

4.0 Conclusion

This study examines an integrated wing-body fusion configuration combining fuselage-section aerofoils and an S-shaped intake, and analysis distributed suction control on the fuselage and coupled internal/external flow control with intake jet injection. Key findings include:

(1) Under cruise conditions, the strong shock wave and intake blockage induce severe adverse pressure gradients, causing massive boundary layer separation. By positioning distributed suction tubes ahead of the shock wave and separation points, uniform near-wall vortex interactions are generated. This effectively redirects high-energy mainstream flow towards the wing surface, energising the boundary layer fluid to resist adverse pressure gradients. Consequently, the ingested boundary layer thickness is significantly reduced, improving the total pressure recovery coefficient.

(2) For thicker upper-surface boundary layers, a dual-row suction configuration outperforms single-row layouts. The optimal control occurs when tubes are positioned pre-shock near the separation initiation points. Compared to parallel layouts, staggered dual-row arrangements induce transverse flows that weaken axial momentum and intensify adverse pressure gradients, thereby triggering premature separation. Under the optimal parallel dual-row layout, the total pressure recovery coefficient (σ) increases by 8% versus the uncontrolled baseline and by 3.1% compared to single-row suction.

(3) Internal intake losses mainly result from two distinct mechanisms: core separation at the lower wall, and secondary swirl induced by centrifugal forces and pressure differentials at the first bend. A partitioned distributed jet strategy effectively decouples their suppression. Central jets introduce high-energy fluid to mitigate core losses, while lateral jets reduce secondary losses through enhanced mixing. Specifically, increasing the central-jet flow ratio to 1.1% improves σ by 1.2%, while a 1.3% lateral-jet flow reduces lower-wall *DC* (150) by 23% and by *SC* (150) 4.6%.

(4) In the synergistic configuration, external wing suction acts as an aerodynamic 'pre-conditioning' for the inflow, significantly alleviating the burden on the internal control system. Thus, internal partition jets can effectively suppress secondary swirl and core separation with minimal momentum. Overall, the coupled control increases the AIP recovery coefficient by 8.3% and reduces total and swirl distortions by 36% and 7.2%, respectively, compared to standalone suction. Energy analysis validates the system-level efficiency, confirming that a 55.5% intake thrust gain is achieved with a minor energy consumption equivalent to only 7.4% of the mainstream kinetic energy.

Acknowledgements. The authors acknowledge the support of the National Key R&D Program of China (2022YFB4301000).

Competing interests. The authors declare that they have no known competing financial interests or personal relationships that could have appeared to influence the work reported in this paper.

https://doi.org/10.1017/aer.2026.10186 Published online by Cambridge University Press

References

[1] Hileman, J., Spakovszky, Z., Drela, M. and Sargeant, M. Aerodynamic and aeroacoustic three-dimensional design for a "silent" aircraft, 44th AIAA Aerospace Sciences Meeting and Exhibit, 2012. https://doi.org/10.2514/6.2006-241

[2] Hall, C.A. and Crichton, D. Engine design studies for a silent aircraft, *ASME. J. Turbomach.*, 2007, **129**, (3), pp 479–487. https://doi.org/10.1115/1.2472398

[3] Hileman, J., Reynolds, T., de la Rosa Blanco, E., Law, T. and Thomas, S. Development of approach procedures for silent aircraft, 45th AIAA Aerospace Sciences Meeting and Exhibit, 2012. https://doi.org/10.2514/6.2007-451

[4] Law, T. and Dowling, A. Optimisation of traditional and blown liners for a silent aircraft, 12th AIAA/CEAS Aeroacoustics Conference (27th AIAA Aeroacoustics Conference), 2012. https://doi.org/10.2514/6.2006-2525

[5] Hileman, J.I., Spakovszky, Z.S., Drela, M., Sargeant, M.A. and Jones, A. Airframe design for silent fuel-efficient aircraft, *J. Aircr.*, 2010, **47**, (3), pp 956–969. https://doi.org/10.2514/1.46545

[6] Plas, A., Crichton, D., Sargeant, M., Hynes, T., Greitzer, E., Hall, C. and Madani, V. performance of a boundary layer ingesting (BLI) propulsion system, 45th AIAA Aerospace Sciences Meeting and Exhibit, 2012. https://doi.org/10.2514/6.2007-450

[7] Kim, H. and Felder, J. Control volume analysis of boundary layer ingesting propulsion systems with or without shock wave ahead of the inlet, 49th AIAA Aerospace Sciences Meeting Including the New Horizons Forum and Aerospace Exposition, 2012. https://doi.org/10.2514/6.2011-222

[8] Felder, J., Kim, H., Brown, G. and Kummer, J. An examination of the effect of boundary layer ingestion on turboelectric distributed propulsion systems, 49th AIAA Aerospace Sciences Meeting Including the New Horizons Forum and Aerospace Exposition, 2012. https://doi.org/10.2514/6.2011-300

[9] Greitzer, E.M., Bonnefoy, P.A., DelaRosaBlanco, E., Dorbian, C.S., Drela, M., Hall, D.K. and Wen, E.A. N+ 3 aircraft concept designs and trade studies (No. E-17419-1), 2010.

[10] Wick, A.T., Hooker, J.R. and Zeune, C.H. Integrated Aerodynamic benefits of distributed propulsion, 53rd AIAA Aerospace Sciences Meeting, 2015. https://doi.org/10.2514/6.2015-1500

[11] Smith, A.M.O. and Roberts, H.E. The jet airplane utilizing boundary layer air for propulsion, *J. Aeronaut. Sci.*, 1947, **14**, (2), pp 97–109. https://doi.org/10.2514/8.1273

[12] Kawai, R.T., Friedman, D.M. and Serrano, L. Blended wing body (BWB) boundary layer ingestion (BLI) inlet configuration and system studies (No. NASA/CR-2006-214534), 2006.

[13] Perry, A.T., Ansell, P.J. and Kerho, M.F. Aero-propulsive and propulsor cross-coupling effects on a distributed propulsion system, *J. Aircr.*, 2018, **55**, (6), pp 2414–2426. https://doi.org/10.2514/1.C034861

[14] Kerho, M.F. Aero-propulsive coupling of an embedded, distributed propulsion system, 33rd AIAA Applied Aerodynamics Conference, 2015. https://doi.org/10.2514/6.2015-3162

[15] Mantič-Lugo, V., Doulgeris, G. and Singh, R. Computational analysis of the effects of a boundary layer ingesting propulsion system in transonic flow, *Proc. Inst. Mech. Eng. Part G*, 2013, **227**, (8), pp 1215–1232. https://doi.org/10.1177/0954410012453390

[16] Kim, H. and Liou, M.S. Flow simulation and optimal shape design of N3-X hybrid wing body configuration using a body force method, *Aerosp. Sci. Technol.*, 2017, **71**, pp 661–674. https://doi.org/10.1016/j.ast.2017.09.046

[17] Kim, H., Liou, M.F. and Liou, M.S. Mail-slot nacelle shape design for N3-X hybrid wing-body configuration, 51st AIAA/SAE/ASEE Joint Propulsion Conference, 2015. https://doi.org/10.2514/6.2015-3805

[18] Xiang, Y., Wu, J. and Xiong, J. Aerodynamic design of nacelle of blended-wing-body aircraft with distributed propulsion, *J. Beijing Univ. Aeronaut. Astronaut.*, 2018, **44** (1), pp 71–81 (in Chinese). https://doi.org/10.13700/j.bh.1001-5965.2017.0027

[19] Ferrar, A. and O'Brien, W. Flow in boundary layer ingesting serpentine inlets, 47th AIAA/ASME/SAE/ASEE Joint Propulsion Conference & Exhibit, 2012. https://doi.org/10.2514/6.2011-5568

[20] Florea, R., Reba, R., Vanslooten, P., Sharma, O., Stucky, M., O'Brien, W. and Arend, D. Preliminary design for embedded engine systems, 47th AIAA Aerospace Sciences Meeting Including The New Horizons Forum and Aerospace Exposition, 2012. https://doi.org/10.2514/6.2009-1131

[21] Thouault, N., Breitsamter, C. and Adams, N.A. Numerical investigation of inlet distortion on a wing-embedded lift fan, *J. Propul. Power*, 2011, **27**, (1), pp 16–28. https://doi.org/10.2514/1.46046

[22] Frohnapfel, D.J. and O'Brien, W.F. Fan response to inlet swirl distortions produced by boundary layer ingesting aircraft configurations. 51st AIAA/SAE/ASEE Joint Propulsion Conference, 2015. https://doi.org/10.2514/6.2015-3804

[23] Vakili, A., Wu, J., Liver, P. and Bhat, M. Flow control in a diffusing S-duct, Shear Flow Control Conference, 2013. https://doi.org/10.2514/6.1985-524

[24] Pradeep, A.M. and Sullerey, R.K. Secondary flow control in a circular S-duct diffuser using vortex generator jets, 2nd AIAA Flow Control Conference, 2012. https://doi.org/10.2514/6.2004-2615

[25] Küçük, U.C., Baran, Ö.U. and Uzol, O. Passive flow control in boundary layer ingesting semi submerged inlet, 51st AIAA/SAE/ASEE Joint Propulsion Conference, 2015. https://doi.org/10.2514/6.2015-3803

[26] Harrison, N.A., Anderson, J., Fleming, J.L. and Ng, W.F. Active flow control of a boundary layer-ingesting serpentine inlet diffuser, *J. Aircr.*, 2013, **50**, (1), pp 262–271. https://doi.org/10.2514/1.C031818

[27] Debiasi, M., Herberg, M., Zeng, Y., Tsai, H.M. and Dhanabalan, S. Control of flow separation in S-ducts via flow injection and suction, 46th AIAA Aerospace Sciences Meeting and Exhibit, 2012. https://doi.org/10.2514/6.2008-74

[28] Duke, D. and Kitsios, V. Flow control in s-shaped air intake using zero-net-mass-flow, 2007.

[29] Wellborn, S., Reichert, B. and Okiishi, T. An experimental investigation of the flow in a diffusing S-duct, 28th Joint Propulsion Conference and Exhibit, 2013. https://doi.org/10.2514/6.1992-3622

https://doi.org/10.1017/aer.2026.10186 Published online by Cambridge University Press

[30] Xu, K. and Zha, G. Distortion elimination for serpentine duct at various Mach numbers using co-flow jet active flow control, *Aerosp. Sci. Technol.*, 2024, **144**, p 108776. https://doi.org/10.1016/j.ast.2023.108776
[31] Xu, K. and Zha, G. System energy benefit using co-flow jet active separation control for a serpentine duct, *Aerosp. Sci. Technol.*, 2022, **128**, p 107746. https://doi.org/10.1016/j.ast.2022.107746
[32] Häberle, J. and Gülhan, A. Investigation of the performance of a scramjet inlet at Mach 6 with boundary layer bleed, 14th AIAA/AHI Space Planes and Hypersonic Systems and Technologies Conference, 2012. https://doi.org/10.2514/6.2006-8139
[33] Sharma, P., Varma, D. and Ghosh, S. Novel vortex generator for mitigation of shock-induced flow separation, *J. Propul. Power*, 2016, **32**, (5), pp 1264–1274. https://doi.org/10.2514/1.B35962
[34] Chakraborty, P., Balachandar, S. and Adrian, R.J. On the relationships between local vortex identification schemes, *J. Fluid Mech.*, 2005, **535**, pp 189–214. https://doi.org/10.1017/S0022112005004726
[35] Wellborn, S., Reichert, B. and Okiishi, T. An experimental investigation of the flow in a diffusing S-duct, 28th Joint Propulsion Conference and Exhibit, 2013. https://doi.org/10.2514/6.1992-3622

Cite this article: Ma B., Liu Y., Li L., Gong T. and Yuan W. (2026). Synergistic flow control for coupled internal–external flows in semi-embedded wing-intake configurations. *The Aeronautical Journal*, **130**, 2528–2557. https://doi.org/10.1017/aer.2026.10186

https://doi.org/10.1017/aer.2026.10186 Published online by Cambridge University Press